Computers and Chemical Engineering 183 (2024) 108612

Contents lists available at ScienceDirect

Computers and Chemical Engineering

journal homepage: www.elsevier.com/locate/cace

Solving crystallization/precipitation population balance models in CADET, part I: Nucleation growth and growth rate dispersion in batch and continuous modes on nonuniform grids

Wendi Zhang[a], Todd Przybycien[a], Johannes Schmölder[b], Samuel Leweke[b], Eric von Lieres[b,*]

[a] Department of Chemical and Biological Engineering, Rensselaer Polytechnic Institute, Troy, 12180, NY, USA
[b] Forschungszentrum Jülich, IBG-1: Biotechnology, Jülich, 52428, Germany

ARTICLE INFO

Keywords:
Precipitation and crystallization
Population balance model
Stirred tank and dispersive plug flow reactors
Finite volumes on nonuniform grid
Analytical Jacobian
Open source CADET software

ABSTRACT

We have developed, implemented and validated 1D and 2D population balance models (PBMs) in the open-source process simulator CADET. 1D PBMs incorporate the particle size as an internal coordinate and are associated with dynamic mass balances to describe particle-based processes in batch and continuous stirred tank reactors. 2D PBMs include the spatial position as an additional external coordinate to describe particulate systems in dispersive plug flow reactors. Along with particle nucleation and growth, growth rate dispersion is considered. Using the finite volume method, cell face fluxes are reconstructed by upwind, Koren and two weighted essentially non-oscillatory (WENO) schemes. Analytical Jacobians are derived to reduce runtime. The implementations utilize arbitrary grids in the internal coordinate. The implementations are validated and benchmarked using seven test cases. The L1 error norm, L1 error convergence rate, and moments up to sixth order are analyzed. Runtime and approximation errors are reported and discussed in detail.

1. Introduction

Precipitation and crystallization represent important processes for the separation and purification of a wide range of fine chemicals, food products, pharmaceuticals and biopharmaceuticals (Randolph and Larson, 1988; Myerson et al., 2002). Both processes are typically performed in batch stirred tank reactors (BSTR) or continuous stirred tank reactors (CSTR) (Wood et al., 2019). More recently continuous operation in dispersive plug flow reactor (DPFR) formats is receiving growing interest (Rothstein, 1993; Li et al., 2019; Burgstaller et al., 2019; Bansode et al., 2022; Alvarez and Myerson, 2010; Jiang and Braatz, 2019). The particle size distribution (PSD) of the final product that exits a crystallization or precipitation reactor has a significant impact on the design and operation of subsequent processing steps, such as settling, centrifugation, filtration, drying, and filling, and may also play an important role in the ultimate performance of the product. Therefore, a powerful and flexible modeling tool is needed for the prediction of PSD in particulate processes.

The population balance model (PBM) is in common use in the description of BSTR- and CSTR-based particulate processes and has been shown to accurately predict the PSD in crystallization processes (Randolph and Larson, 1988; Myerson et al., 2002). The PBM is at heart a continuity equation following a mass conservation law combined with a set of nucleation and growth kinetic equations that, combined together, are able to track the behaviors of a dynamic particle population as a whole (Randolph and Larson, 1988; Hulburt and Katz, 1964). Despite their relatively simple construction, the governing equations themselves are hard to solve. There are special conditions where the PBM may be solved analytically, but these conditions are of minimal practical use. Through the effort of many researchers over the last three decades, several algorithms for solving the PBM have been established. Widely used algorithms can be broadly categorized into three types: the method of moments (Smith and Matsoukas, 1998; Marchisio et al., 2003; Yuan et al., 2012), discretization methods (Gunawan et al., 2004; Bennett and Rohani, 2001; Qamar et al., 2009) and Monte Carlo methods (Smith and Matsoukas, 1998; Lin et al., 2002). Less common algorithms have also been used and include the spectrum method (Mantzaris et al., 2001), the Lattice Boltzmann method (Majumder et al., 2012) and the method of characteristics (Pilon and Viskanta, 2003). The discretization methods, including finite difference, finite volume, and finite element methods, are universal methods for solving partial differential equations. Discontinuous Galerkin methods belong to the class of finite element methods and have also been applied to the solution of the PBM (Ahmed et al., 2011).

---

* Corresponding author.
E-mail address: e.von.lieres@fz-juelich.de (E. von Lieres).

https://doi.org/10.1016/j.compchemeng.2024.108612
Received 3 November 2023; Received in revised form 18 January 2024; Accepted 21 January 2024

Among all the algorithms, the finite volume method stands out as the most documented and used method for solving the PBM. The finite difference method is easy to implement but may not be the best choice for the PBM because it is not mass preserving. In addition, it can introduce relatively strong numerical diffusion, leading to artificial broadening of the distribution (Mahoney and Ramkrishna, 2002) and larger errors compared with the finite volume method (Gunawan et al., 2004). Contrary to the finite difference and finite volume methods, the finite element and discontinuous Galerkin methods are rather complex. Furthermore, comparative studies have shown that the latter methods can have poor performance when sharp moving fronts, which may be introduced by fast and nonlinear growth rates, are present (Mesbah et al., 2009). Compared to these methods, the finite volume method has several advantages: 1. the implementation is not difficult; 2. it suits the hyperbolic nature of the PBM; 3. it fully recovers the PSD; 4. mass is always conserved; and 5. boundary conditions enter finite volume discretizations naturally.

Using the finite volume method, Gunawan et al. (2004) tested a high-resolution scheme with a flux limiter based on LeVeque's analysis of hyperbolic equations (LeVeque, 2002). Qamar et al. (2006) carried out a numerical analysis on another finite volume high-resolution scheme originally developed by Barry (1993). Both schemes have been shown to offer excellent accuracy when used with a uniform grid. However, using a nonuniform grid can improve the computational efficiency by requiring fewer cells, particularly when the experimental PSD data are reported on a nonuniform grid. Unfortunately, the original high-resolution scheme uses an unmodified van Leer flux limiter that is not valid on nonuniform grids. In addition to high-resolution schemes, and instead of using flux limiters to limit the numerical flux, the weighted essentially non-oscillatory (WENO) scheme, which focuses on an essentially non-oscillatory flux reconstruction, is also a promising candidate for solving the PBM (Liu et al., 1994; Jiang and Shu, 1996; Harten et al., 1987). Lim et al. (2002) found that the finite volume WENO scheme was superior to the methods of characteristics in terms of resolving steep PSD fronts and discontinuities. Hermanto et al. (2009) compared WENO schemes with a high-resolution scheme and a finite difference scheme on a uniform grid and concluded that the WENO scheme is well suited to solve the PBM as it exhibited an average error convergence rate of 2.59 as well as a short runtime. However, contrary to its simple expressions on uniform grids, which aided its popularity, WENO formulations on a nonuniform grid are rather complex.

The PBM commonly employs constitutive particle nucleation and growth equations which are often tested together. In addition to the most commonly seen situation where the nucleation processes generate particles as mono-sized critical nuclei, particles may be born beyond the critical nuclei size (Ramkrishna, 2000), a situation that has not been investigated numerically. Apart from nucleation and growth processes, several recent publications direct the community's attention to the modeling of growth rate dispersion (Myerson et al., 2002; Alvarez and Myerson, 2010; Srisanga et al., 2015; Benitez-Chapa et al., 2020). According to Randolph and Larson (1988), the random fluctuation that occurs around the mean particle size can be represented by a second order term resembling molecular diffusion. Even though this approach is widely accepted now, its numerical aspects have not yet been studied by any finite volume method based PBM analysis.

The analyses above are based on the one-dimensional formulation of the PBM which is suitable for the simulation of well-mixed BSTR and CSTR based operations. Unfortunately, the 1D PBM falls short when newer process formats based on dispersive plug flow reactors (DPFRs) are used. Here, a multi-dimensional PBM is needed to include one or more spatial reactor dimensions. We have formulated a two-dimensional population balance model (2D PBM) for the DPFR format which incorporates both an internal particle size coordinate and an external spatial (axial) coordinate. The lack of a convenient 2D PBM design tool with associated comprehensive numerical analysis and validation motivated us to implement and test a 2D PBM that is specifically formulated for DPFRs.

Both the 1D and 2D PBMs are implemented and tested in CADET (von Lieres and Andersson, 2010; Leweke and von Lieres, 2018), a modular, free and open-source process modeling software package that has a C++ numerical core and can be easily accessed from a user-friendly Python environment. CADET was originally developed as a fast and accurate numerical solver for the mechanistic modeling of chromatographic processes, but it has been actively developed and extended in recent years to tackle numerical challenges in the modeling of crystallization, filtration, and fermentation processes. CADET consists of a large network of unit operations including reactors, pumps, valves, tubes, tanks, and uses state-of-the-art algorithms and scientific computing techniques to efficiently solve differential–algebraic equations. CADET uses the backward differential formula (BDF) implemented in the implicit differential–algebraic solver (IDAS) as the time integrator. Application of the BDF to the discretized PBM yields a nonlinear algebraic equation system that is solved using Newton iterations. During each Newton iteration, IDAS expects a Jacobian to be provided. Automatic Differentiation (AD) is employed to provide the Jacobian and has been implemented in CADET in a previous release (Leweke and von Lieres, 2018). To reduce the runtime, we also provide IDAS with an analytical Jacobian. Symbolic expressions of the analytical Jacobian are dependent on the solution schemes used for the internal and external coordinates and, especially when a nonuniform grid is used, can be very complicated.

The purpose of this research work is to 1. carry out a thorough numerical analysis on the 1D and 2D PBMs; 2. implement, validate and benchmark numerical schemes for the 1D and 2D PBMs in the modular, free and open-source process modeling package CADET; 3. compare these schemes in terms of their accuracy and efficiency under different conditions and provide guidance on how to identify a reliable, efficient and robust method. Overall, this work aims to provide references and new insights into: PBM formulations for BSTR, CSTR and DPFR formats; numerical approximations applied to the growth rate dispersion; and finite volume methods using high order flux reconstructions on a nonuniform grid and their associated analytical Jacobians.

2. The population balance model

2.1. Governing equations

The population balance model is a widely used mathematical framework for modeling crystallization and precipitation processes. The population balance equation is a particle-number continuity equation which describes the evolution of the number density n of particles in the time and space domains. The particles of interest have both internal and external coordinates: the internal coordinate can be chosen as any property of the particles such as the particle size or volume, while the external coordinate can be a characteristic dimension of the reactor itself, including the axial position. Although each coordinate can constitute a variety of characteristic properties of particles and reactors, the most common choice is to use a particle size x as the internal coordinate for spatially uniform reactor format cases like BSTRs or CSTRs, or adding an axial position z as the external coordinate to account for spatial variations in the DPFR case.

2.1.1. PBM in a batch or continuous stirred-tank reactor (BSTR or CSTR)

The one-dimensional population balance for a well-mixed reactor, including particle nucleation and growth processes as well as growth rate dispersion, is

$$\frac{\partial(nV)}{\partial t} = F_{in}n_{in} - F_{out}n - V\left(\frac{\partial(v_G n)}{\partial x} - D_g\frac{\partial^2 n}{\partial x^2} - B_0 P\right) \tag{1}$$

where F_{in} and F_{out} are the volumetric inflow and outflow rates, V is the reactor volume, n is the number density, n_{in} is the inlet number density distribution, v_G is the particle growth rate, D_g is an empirically defined growth dispersion rate which will be discussed in the next section, B_0 is the nucleation kinetics and $P = P(x)$ is the probability density function of the particles generated by nucleation. A special case is that when the particles are born as mono-sized critical nuclei (Randolph and Larson, 1988), rendering

$$\frac{\partial(nV)}{\partial t} = F_{in}n_{in} - F_{out}n - V\left(\frac{\partial(v_G n)}{\partial x} - D_g\frac{\partial^2 n}{\partial x^2} - B_0\delta(x - x_c)\right) \tag{2}$$

where P becomes the Dirac delta function δ and x_c is the critical nucleus size. This is the most commonly seen case in the literature. The above two equations are valid in the absence of particle aggregation and breakage processes.

The corresponding upper boundary condition for both cases is called the regularity boundary condition: it states that the total flux in the internal coordinate vanishes for particles of infinite sizes (Ramkrishna, 2000):

$$\left(nv_G - D_g\frac{\partial n}{\partial x}\right)\Big|_{x\to\infty} = 0. \tag{3}$$

The lower boundary condition for Eq. (1) is

$$\left(nv_G - D_g\frac{\partial n}{\partial x}\right)\Big|_{x=x_{min}} = 0, \tag{4}$$

where x_{min} is the minimum particle size considered. If particles are born as critical nuclei, they enter the particle coordinate through the Dirac delta function. Mathematically, Eq. (2) is equivalent to the following PDE with a nucleation boundary condition at x_c that treats nuclei as a point source:

$$\frac{\partial(nV)}{\partial t} = F_{in}n_{in} - F_{out}n - V\left(\frac{\partial(v_G n)}{\partial x} - D_g\frac{\partial^2 n}{\partial x^2}\right), \tag{5}$$

$$\left(nv_G - D_g\frac{\partial n}{\partial x}\right)\Big|_{x=x_c} = B_0. \tag{6}$$

The initial condition can be any arbitrary distribution for both cases: $n|_{t=0} = n_0$, where n_0 can be a Gaussian, Log-normal, Gamma, or other distribution.

If the solute concentration c in the bulk phase is of interest, Eq. (1) can be coupled with a solute mass balance equation:

$$\frac{\partial(cV)}{\partial t} = F_{in}c_{in} - F_{out}c - \rho k_v V\int_{x_{min}}^{\infty} B_0Px^3 + 3v_G nx^2\,\mathrm{d}x, \tag{7}$$

where c is the solute mass concentration, c_{in} is the inlet solute mass concentration, ρ is the nuclei mass density and k_v is the volumetric shape factor of the particles. The first term inside the integral accounts for the solute mass consumed by nucleation and the second term accounts for the solute mass consumed by particle growth. It is worth mentioning that the solute mass concentration is based on the total volume instead of the solid-free volume. If particles are born as critical nuclei, the mass balance equation becomes (Randolph and Larson, 1988; Nagy et al., 2008):

$$\frac{\partial(cV)}{\partial t} = F_{in}c_{in} - F_{out}c - \rho k_v V\left(B_0x_c^3 + 3\int_{x_c}^{\infty} v_G n\,x^2\,\mathrm{d}x\right). \tag{8}$$

The initial condition for the mass balance in both cases is $c|_{t=0} = c_0$, where c_0 is the initial solute mass concentration in the reactor.

Lastly, if the inflow and outflow rates are different, an auxiliary equation to track the evolution of the reactor's volume is included and solved along with above equations:

$$\frac{\mathrm{d}V}{\mathrm{d}t} = F_{in} - F_{out}. \tag{9}$$

2.1.2. PBM in a dispersive plug flow reactor (DPFR)

If we choose the axial position within a plug flow reactor as the external coordinate z, the 2D PBM incorporating axial dispersion is

$$\frac{\partial n}{\partial t} = -v_{ax}\frac{\partial n}{\partial z} + D_{ax}\frac{\partial^2 n}{\partial z^2} - \frac{\partial(v_G n)}{\partial x} + D_g\frac{\partial^2 n}{\partial x^2} + B_0P, \tag{10}$$

where v_{ax} is the axial velocity, D_{ax} is the axial dispersion coefficient and $P = P(x)$ is the probability density function of the particles generated by nucleation. The above equation assumes that nucleation can happen at any position inside the reactor. If the particles are born as critical nuclei, then P becomes a Dirac delta function:

$$\frac{\partial n}{\partial t} = -v_{ax}\frac{\partial n}{\partial z} + D_{ax}\frac{\partial^2 n}{\partial z^2} - \frac{\partial(v_G n)}{\partial x} + D_g\frac{\partial^2 n}{\partial x^2} + B_0\delta(x - x_c). \tag{11}$$

The lower and upper boundary conditions for the internal coordinate are the same as those for the 1D PBM as show in Eqs. (3) and (4).

In the critical nuclei birth case, the Dirac delta function in Eq. (11) can be eliminated by using a nucleation boundary condition for the internal coordinate, leading to

$$\frac{\partial n}{\partial t} = -v_{ax}\frac{\partial n}{\partial z} + D_{ax}\frac{\partial^2 n}{\partial z^2} - \frac{\partial(v_G n)}{\partial x} + D_g\frac{\partial^2 n}{\partial x^2} \tag{12}$$

with the updated boundary condition given by Eq. (6).

For the external coordinate z, Danckwerts boundary conditions are applied:

$$\left(nv_{ax} - D_{ax}\frac{\partial n}{\partial z}\right)\Big|_{z=0} = v_{ax}n_{in,x}, \qquad \frac{\partial n}{\partial z}\Big|_{z=L} = 0, \tag{13}$$

where L is the length of the DPFR. The initial condition for the 2d PBM is given by $n|_{t=0} = n_0$, where n_0 is the initial distribution of the seed particles.

The particle population balance Eq. (11) can again be coupled to the solute mass balance equation:

$$\frac{\partial c}{\partial t} = -v_{ax}\frac{\partial c}{\partial z} + D_{ax}\frac{\partial^2 c}{\partial z^2} - \rho k_v\int_{x_{min}}^{\infty} B_0Px^3 + 3v_G nx^2\,\mathrm{d}x. \tag{14}$$

If particles are born as critical nuclei, Eq. (10) is coupled to the following mass balance equation:

$$\frac{\partial c}{\partial t} = -v_{ax}\frac{\partial c}{\partial z} + D_{ax}\frac{\partial^2 c}{\partial z^2} - \rho k_v\left(B_0x_c^3 + 3\int_{x_c}^{\infty} v_G nx^2\,\mathrm{d}x\right). \tag{15}$$

As with the particle phase, the solute mass concentration c is also subject to the Danckwerts boundary conditions

$$\left(cv_{ax} - D_{ax}\frac{\partial c}{\partial z}\right)\Big|_{z=0} = v_{ax}c_{in}, \qquad \frac{\partial c}{\partial z}\Big|_{z=L} = 0. \tag{16}$$

The initial condition for the mass balance is $c|_{t=0} = c_0$, where c_0 is the initial spatial mass concentration distribution of the solute in the reactor.

2.2. Constitutive equations

Constitutive equations describe the nucleation and growth kinetic processes in the governing equations. Most of these relations have been widely used to describe crystallization processes (Randolph and Larson, 1988; Myerson et al., 2002) and are assumed to be applicable to precipitation processes (Raphael and Rohani, 1999; Marchal et al., 1988). The solute starts to precipitate or crystallize when the solute concentration exceeds its solubility in the solvent. Supersaturated solutions can be created by changing the temperature, evaporating the solvent or adding an anti-solvent. The extent of supersaturation provides the driving force for the nucleation and growth processes. We define a relative supersaturation s as

$$s = \frac{c - c_{eq}}{c_{eq}},$$

where c_{eq} is the solute solubility in the solvent.

New particles are formed through primary and secondary nucleation mechanisms. Primary nucleation refers to nuclei formation when no suspended particles are present while secondary nucleation refers to nuclei formation around other particles or in contact with the reactor vessel surfaces (Randolph and Larson, 1988). An empirical equation for primary nucleation is frequently used:

$$B_p = k_p s^u,$$

where k_p is the primary nucleation rate constant and u is a constant. Regarding secondary nucleation, an empirical power-law expression that is frequently used in the literature (Randolph and Larson, 1988) is considered:

$$B_s = k_b s^b M,$$

where k_b is the secondary nucleation rate constant, b is a system-related parameter and M is the suspension density. A higher suspension density provides a higher collision rate and, therefore, greater effectiveness for secondary nucleation mechanisms (Randolph and Larson, 1988). M is defined as

$$M = k_v \rho \int_0^{\infty} n\ x^3\ \mathrm{d}x.$$

Some authors use the volume fraction ϕ to replace the suspension density M. The two can be easily inter-converted using $M = \rho\phi$. The total nucleation rate is the sum of the primary and secondary nucleation rates:

$$B_0 = B_p + B_s.$$

Note that there is no convincing evidence that secondary nucleation takes place when particles are nucleated at sizes larger than the critical nuclei size. Hence, secondary nucleation is generally ignored in this case.

Particle growth can generally be defined as the process in which solutes are transported to the particle surface and then oriented and incorporated into the particle lattice (Myerson et al., 2002). Current models can be classified into size-independent or size-dependent growth models. A size-dependent growth mechanism was proposed based on the idea that as the particle becomes larger, its total surface area increases, increasing the probability of occurrence of dislocations on the surface (Garside and Jančić, 1976). A general expression for the growth rate incorporating both size-independent and size-dependent mechanisms is given by

$$v_G = k_g s^g (a + \gamma x)^p,$$

where k_g is the growth rate constant, γ quantifies the size dependence, and g, a and p are system-related constants. If $a = 1$, the model becomes the three-parameter Abegg's model (Abegg et al., 1968), if $a = 0$ and $\gamma = 1$, this model reduces to Bransom's model, if $a = p = 1$, this model becomes Canning and Randolph's model (Canning and Randolph, 1967). For size-independent growth, setting $\gamma = 0$ and $p = 0$ results in $v_G = k_g s^g$. This is also known as *McCabe's ΔL law* (McCabe, 1929).

Growth rate dispersion is another phenomenon closely associated with size-dependent growth. This concept originates in experimental observations of particle growth processes, where particles of the same sizes and compositions exposed to identical temperature, supersaturation and hydrodynamic conditions do not necessarily grow at the same rate (Randolph and White, 1977). This is not the same as size-dependent growth, in which the growth rate of particles of different sizes can be experimentally measured to be different. Two theories have been proposed to explain growth rate dispersion. The first posits that nuclei are born with an intrinsic distribution of growth rates (Larson et al., 1985). The second proposes that particles display the same time-averaged growth rate, but that the growth rate of each individual particle may fluctuate as a function of time (Randolph and White, 1977). The second theory has led to the formulation of PBMs with a dispersion term in the internal coordinate (Eq. (2), the second term on the right hand side): according to Randolph and Larson (1988), the spreading of the PSD due to random fluctuations in the growth rate can be represented as a dispersive flux in response to a gradient in the size distribution, analogous to a molecular diffusion flux due to a spatial concentration gradient. There are other underlying mechanisms hypothesized to explain growth rate dispersion (Larson et al., 1985), but they are rarely used in the current literature. Since our primary aim is to investigate the numerical aspects of the PBM, not the physical nature of the phenomenon, we focus on the dispersive flux formulation of this process (Myerson et al., 2002; Alvarez and Myerson, 2010; Srisanga et al., 2015).

The last piece of the PBM is the solubility model. The solubility c_{eq} often depends on temperature or anti-solvent concentration. Well-known solubility theories and models include, but are not limited to, regular solution theory and the NRTL, UNIQUAC, COSMO-RS models among others (Myerson et al., 2002). Semi-empirical models such as the Cohn–Setschenow equation are often used in precipitation processes (Gu et al., 2020). The specific functional dependence of the solubility model is highly dependent on the nature of the crystallization or precipitation system and it is difficult to give a general expression for all applications. To facilitate the future implementation of the external dependence of the solubility, we treat the solubility as a separate pseudo-component of the solution having a concentration c_{eq}.

3. Finite volume method discretization

3.1. One dimensional discretization: internal coordinate x

In this section, we apply the cell-centered finite volume method to discretize Eqs. (1) and (5). First, we truncate the upper bound from infinity to a sufficiently large number x_{max} and discretize between x_{min} and x_{max}, obtaining: $x_{min} = x_{1/2} < x_{3/2} < \cdots < x_{N_x-1/2} < x_{N_x+1/2} = x_{max}$, where N_x is the total number of cells for the internal coordinate. For the most common situation where all particles are nucleated as critical nuclei, x_{min} is usually chosen as x_c. The size of cell i is denoted by $\Delta x_i = x_{i+1/2} - x_{i-1/2}$ and its center is defined as $x_i = (x_{i+1/2} + x_{i-1/2})/2$.

Applying the product rule to the temporal derivative and the cell-centered finite volume discretization to Eq. (1), we obtain

$$\begin{gathered}\int_{x_{i-1/2}}^{x_{i+1/2}} \left(n\frac{\partial V}{\partial t} + V\frac{\partial n}{\partial t} \right) \mathrm{d}x = \\ \int_{x_{i-1/2}}^{x_{i+1/2}} F_{in} n_{in} - F_{out} n\ \mathrm{d}x + \int_{x_{i-1/2}}^{x_{i+1/2}} B_0 P V\ \mathrm{d}x \\ + \left(-\left.(v_G n)\right|_{x_{i+1/2}} + \left.(v_G n)\right|_{x_{i-1/2}} + D_g \left.\frac{\partial n}{\partial x}\right|_{x_{i+1/2}} - D_g \left.\frac{\partial n}{\partial x}\right|_{x_{i-1/2}} \right) V,\end{gathered} \tag{17}$$

where $\left.(v_G n)\right|_{x_{i\pm1/2}}$ and $D_g \left.\frac{\partial n}{\partial x}\right|_{x_{i\pm1/2}}$ are the convective and diffusive fluxes at cell faces $x_{i\pm1/2}$, respectively. Defining the cell average number density n_i as

$$n_i = \frac{1}{\Delta x_i} \int_{x_{i-1/2}}^{x_{i+1/2}} n\ \mathrm{d}x \tag{18}$$

and approximating P and n_{in} via the midpoint quadrature rule $\int_{x_{i-1/2}}^{x_{i+1/2}} P\ \mathrm{d}x \approx P(x_i)\Delta x_i$ and $\int_{x_{i-1/2}}^{x_{i+1/2}} n_{in}\ \mathrm{d}x \approx n_{in}(x_i)\Delta x_i$, Eq. (17) becomes

$$\begin{gathered} n_i \frac{\partial V}{\partial t} + V\frac{\partial n_i}{\partial t} = F_{in} n_{in,i} - F_{out} n_i + B_0 P_i V \\ + \left(-\frac{\left.(v_G n)\right|_{x_{i+1/2}} - \left.(v_G n)\right|_{x_{i-1/2}}}{\Delta x_i} + D_g \frac{\left.\frac{\partial n}{\partial x}\right|_{x_{i+1/2}} - \left.\frac{\partial n}{\partial x}\right|_{x_{i-1/2}}}{\Delta x_i} \right) V,\end{gathered} \tag{19}$$

where $P_i = P(x_i)$ and $n_{in,i} = n_{in}(x_i)$. The approximation P_i of the source term P is second-order accurate. While higher order reconstructions of the source term P are possible, they are not considered in this study because finite volume methods for other terms are usually limited to second order (Xing and Shu, 2006). For simplicity, we denote the fluxes evaluated at the cell faces as

$$F_{i+1/2} = \left.(v_G n)\right|_{x_{i+1/2}}, \qquad \Lambda_{i+1/2} = D_g \left.\frac{\partial n}{\partial x}\right|_{x_{i+1/2}}. \tag{20}$$

Therefore, Eq. (19) becomes

$$n_i \frac{\partial V}{\partial t} + V \frac{\partial n_i}{\partial t} = F_{in} n_{in,i} - F_{out} n_i + B_0 P_i V \\ + \left(-\frac{F_{i+1/2} - F_{i-1/2}}{\Delta x_i} + \frac{\Lambda_{i+1/2} - \Lambda_{i-1/2}}{\Delta x_i} \right) V. \tag{21}$$

Finite volume discretization of Eq. (2) is performed similarly and gives

$$n_i \frac{\partial V}{\partial t} + V \frac{\partial n_i}{\partial t} = F_{in} n_{in,i} - F_{out} n_i \\ + \left(-\frac{F_{i+1/2} - F_{i-1/2}}{\Delta x_i} + \frac{\Lambda_{i+1/2} - \Lambda_{i-1/2}}{\Delta x_i} \right) V. \tag{22}$$

Eqs. (21), (22) along with (9) are the implementation-ready governing equations of the 1D PBM, depending on the treatment of the nucleation source term.

The diffusive flux is approximated by the central difference quotient which is second order on uniform grids

$$\Lambda_{i+1/2} \approx \tilde{\Lambda}_{i+1/2} = D_g \frac{n_{i+1} - n_i}{x_{i+1} - x_i} = D_g \frac{n_{i+1} - n_i}{\Delta' x_i}, \tag{23}$$

where $\Delta' x_i$ is the distance between the ith and $(i+1)$th cell center $\Delta' x_i = x_{i+1} - x_i$. On nonuniform grids, it becomes first order accurate. Higher order approximation of the diffusive flux is possible (Nishikawa, 2014; Calhoun and LeVeque, 2000) and can be included in future work, but it is not necessary since, in the most prevalent case where particles are born as critical nuclei, the discretization order is limited to a maximum second order due to the boundary treatment and to flux limiting. Approximation of the convective flux $F_{i+1/2}$ by the numerical flux $\tilde{F}_{i+1/2}$ is performed using several different schemes which are discussed in the next section.

It is clear from Eq. (23) that one upwind and one downwind cell must be evaluated to estimate the numerical diffusive flux $\tilde{\Lambda}_{i+1/2}$. A natural problem occurs when dealing with cells located at the domain boundaries: to evaluate the first cell, for instance, the average number density in the zeroth cell, which does not exist, is required. Therefore, cells at the domain boundaries must be evaluated using the boundary conditions. At the domain boundaries where $i = 1$ and $i = N_x$, Eq. (21) reads

$$n_1 \frac{\partial V}{\partial t} + V \frac{\partial n_1}{\partial t} = \left(-\frac{\tilde{F}_{3/2}}{\Delta x_1} + \frac{\tilde{\Lambda}_{3/2}}{\Delta x_1} \right) V + B_0 P_1 V,$$

$$n_{N_x} \frac{\partial V}{\partial t} + V \frac{\partial n_{N_x}}{\partial t} = \left(\frac{\tilde{F}_{N_x-1/2}}{\Delta x_{N_x}} - \frac{\tilde{\Lambda}_{N_x-1/2}}{\Delta x_{N_x}} \right) V,$$

after replacing the exact fluxes with their numerical counterparts. Similarly, if particles are born as critical nuclei, Eq. (22) gives

$$n_1 \frac{\partial V}{\partial t} + V \frac{\partial n_1}{\partial t} = \left(\frac{\tilde{F}_{3/2} - B_0}{\Delta x_1} + \frac{\tilde{\Lambda}_{3/2}}{\Delta x_1} \right) V,$$

$$n_{N_x} \frac{\partial V}{\partial t} + V \frac{\partial n_{N_x}}{\partial t} = \left(\frac{\tilde{F}_{N_x-1/2}}{\Delta x_{N_x}} - \frac{\tilde{\Lambda}_{N_x-1/2}}{\Delta x_{N_x}} \right) V.$$

These are the final equations for cells near the boundary of the x domain to be implemented for the 1D PBM in CADET, depending on the nature of the nucleation.

Finally, we discretize the accompanying solute mass balance equation. The integral in the mass balance equation is first truncated from infinity to x_{max} and then approximated by the midpoint quadrature rule. The mass balance Eqs. (7) and (8) give, respectively:

$$c \frac{\partial V}{\partial t} + V \frac{\partial c}{\partial t} = F_{in} c_{in} - F_{out} c \\ -\rho k_v V \sum_{j=1}^{N_x} \left(B_0 P_j x_j^3 \Delta x_j + 3 \upsilon_{G,j} n_j x_j^2 \Delta x_j \right), \tag{24}$$

$$c \frac{\partial V}{\partial t} + V \frac{\partial c}{\partial t} = F_{in} c_{in} - F_{out} c - \rho k_v V \left(B_0 x_c^3 + 3 \sum_{j=1}^{N_x} \upsilon_{G,j} n_j x_j^2 \Delta x_j \right),$$

where $\upsilon_{G,j} = k_g s^g (a + \gamma x_j)^p$. Note that B_0 contains another integral present in M, which is also approximated using a midpoint quadrature rule: $M \approx \rho k_v \sum_{j=1}^{N_x} n_j x_j^3 \Delta x_j$.

3.2. Two dimensional discretization: internal coordinate x and external coordinate z

In this section, we apply the finite volume method to the 2D PBM for a DPFR (Eqs. (10) and (12)). A basic assumption we make from here on is that, except for the number density n, parameters and variables formulated in one coordinate are not explicitly dependent on the other coordinate such that the governing equation can be discretized in the two coordinates separately. For instance, the primary nucleation kinetics $B_p(x, z) = k_p s^u$ does not explicitly depend on the axial coordinate z, but only implicitly through the depletion of the relative supersaturation s, which does depend on the axial position. Bearing this assumption in mind, the internal coordinate x can be discretized as introduced in the section above. The external coordinate z is analogously discretized as: $0 = z_{1/2} < z_{3/2} < \cdots < z_{N_{col}-1/2} < z_{N_{col}+1/2} = L$, where N_{col} is the total number of cells for the external domain z. The size, center and distance between two adjacent centers in the external coordinate cells are defined similarly to those in the internal coordinate: $\Delta z_j = z_{j+1/2} - z_{j-1/2}$, $z_i = (z_{i+1/2} + z_{i-1/2})/2$, $\Delta' z_i = z_{i+1} - z_i$.

To derive the discretized versions of the governing equations for the 2D PBM described by Eqs. (10) and (12), we define the two dimensional cell average as

$$n_{i,j} = \frac{1}{\Delta x_i \Delta z_j} \int_{z_{j-1/2}}^{z_{j+1/2}} \int_{x_{i-1/2}}^{x_{i+1/2}} n \, \mathrm{d}x \, \mathrm{d}z,$$

where the first subscript i is the index for elements in the x coordinate and the second subscript j is the index for elements in the z coordinate. Performing the steps presented in the preceding section, the corresponding implementation-ready discretized 2D PBMs are:

$$\frac{\partial n_{i,j}}{\partial t} = -\frac{\tilde{F}_{i,j+1/2} - \tilde{F}_{i,j-1/2}}{\Delta z_j} + \frac{\tilde{\Lambda}_{i,j+1/2} - \tilde{\Lambda}_{i,j-1/2}}{\Delta z_j} \\ -\frac{\tilde{F}_{i+1/2,j} - \tilde{F}_{i-1/2,j}}{\Delta x_i} + \frac{\tilde{\Lambda}_{i+1/2,j} - \tilde{\Lambda}_{i-1/2,j}}{\Delta x_i} + B_{0,j} P_i, \tag{25}$$

and

$$\frac{\partial n_{i,j}}{\partial t} = -\frac{\tilde{F}_{i,j+1/2} - \tilde{F}_{i,j-1/2}}{\Delta z_j} + \frac{\tilde{\Lambda}_{i,j+1/2} - \tilde{\Lambda}_{i,j-1/2}}{\Delta z_j} \\ -\frac{\tilde{F}_{i+1/2,j} - \tilde{F}_{i-1/2,j}}{\Delta x_i} + \frac{\tilde{\Lambda}_{i+1/2,j} - \tilde{\Lambda}_{i-1/2,j}}{\Delta x_i}, \tag{26}$$

where the convective and diffusive numerical fluxes for the internal coordinate, $\tilde{F}_{i+1/2,j}$ and $\tilde{\Lambda}_{i+1/2,j}$, are defined as in the previous section and approximate the exact fluxes of Eq. (20) at $z = z_j$. $B_{0,j}$ denotes B_0 evaluated at $z = z_j$. The analogous numerical fluxes for the external coordinate $\tilde{F}_{i,j+1/2}$ and $\tilde{\Lambda}_{i,j+1/2}$ are, respectively, defined by

$$\tilde{F}_{i,j+1/2} \approx F_{i,j+1/2} = (\upsilon_{ax} n)\big|_{x_i, z_{j+1/2}}, \tag{27}$$

and

$$\tilde{\Lambda}_{i,j+1/2} = D_{ax} \frac{n_{i,j+1} - n_{i,j}}{\Delta' z_j} \approx \Lambda_{i,j+1/2} = \left. \frac{\partial n}{\partial z} \right|_{x_i, z_{j+1/2}}, \tag{28}$$

where, again, the convective numerical flux $\tilde{F}_{i,j+1/2}$ is described in the next section.

Cells near the domain boundary require special treatment. To facilitate discussion, the 2D discretization scheme, numerical fluxes at the cell faces, and line sources for the 2D PBM are shown graphically in Fig. 1. For 2D problems, there are in total eight special cases representing four vertical and horizontal lines that are the boundary conditions for each coordinate and four points at the intersections of these lines: $\frac{\partial n_{i,1}}{\partial t}$, $\frac{\partial n_{i,N_{col}}}{\partial t}$, $\frac{\partial n_{1,j}}{\partial t}$, $\frac{\partial n_{N_x,j}}{\partial t}$, $\frac{\partial n_{1,1}}{\partial t}$, $\frac{\partial n_{1,N_{col}}}{\partial t}$, $\frac{\partial n_{N_x,1}}{\partial t}$, and $\frac{\partial n_{N_x,N_{col}}}{\partial t}$. Their corresponding expressions are derived in a way similar to that

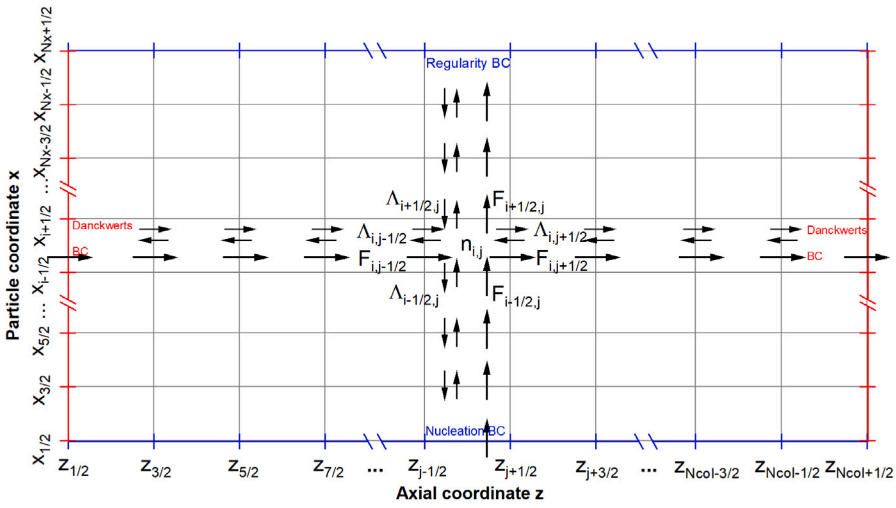

Fig. 1. The regular quadrilateral grid for the two-dimensional cell-centered FVM flux reconstruction. The growth and axial convection numerical fluxes at the cell faces are unidirectional and denoted by longer arrows. Axial dispersion and growth rate dispersion are bidirectional and denoted by smaller double arrows.

in the last section. To avoid redundancy, they are provided in the supplementary information (SI).

The mass balance equation has only one spatial coordinate z. Accordingly, the discretized mass balance Eqs. (14) and (15) read

$$\frac{\partial c_j}{\partial t} = -\frac{\tilde{F}'_{j+1/2} - \tilde{F}'_{j-1/2}}{\Delta z_j} + \frac{\tilde{\Lambda}'_{j+1/2} - \tilde{\Lambda}'_{j-1/2}}{\Delta z_j} - \rho k_v \sum_{j=1}^{N_x} \left(B_{0,j} P_j x_j^3 \Delta x_j + 3 v_{G,j} n_j x_j^2 \Delta x_j \right), \tag{29}$$

and

$$\frac{\partial c_j}{\partial t} = -\frac{\tilde{F}'_{j+1/2} - \tilde{F}'_{j-1/2}}{\Delta z_j} + \frac{\tilde{\Lambda}'_{j+1/2} - \tilde{\Lambda}'_{j-1/2}}{\Delta z_j} - \rho k_v \left(B_{0,j} x_c^3 + 3 \sum_{i=1}^{N_x} v_{G,i} n_i x_i^2 \Delta x_i \right), \tag{30}$$

where the numerical convective and diffusive fluxes in the spatial coordinate $\tilde{F}'_{j+1/2}$ and $\tilde{\Lambda}'_{j+1/2}$ are defined by

$$\tilde{F}'_{j+1/2} \approx \left. (v_{ax} c_j) \right|_{z_{j+1/2}}, \tag{31}$$

and

$$\tilde{\Lambda}'_{j+1/2} = D_{ax} \frac{c_{j+1} - c_j}{\Delta' z_j} \approx D_{ax} \left. \frac{\partial c_j}{\partial z} \right|_{z_{j+1/2}}, \tag{32}$$

where the superscript $'$ is used to further distinguish $\tilde{F}'_{j+1/2}$ and $\tilde{\Lambda}'_{j+1/2}$ from $\tilde{F}_{i,j+1/2}$ and $\tilde{\Lambda}_{i,j+1/2}$. Cells near the domain boundaries are treated similarly to the description above and can be found in the SI.

4. Flux reconstruction on uniform and nonuniform grids

In this section, we introduce the methods used to estimate the numerical convective flux $\tilde{F}_{i+1/2}$. While the development below employs n to illustrate the algorithms for use in the 1D and 2D population balance equations, n may be exchanged for c for use in the associated mass balance equation.

4.1. Upwind scheme

When using an upwind scheme, $\tilde{F}_{i+1/2}$ can be directly calculated from the cell average of an upwind cell:

$$\tilde{F}_{i+1/2} = \tilde{F}_{upwind,i+1/2} = v_{G,i+1/2} n_i \tag{33}$$

where $v_{G,i+1/2}$ is given by:

$$v_{G,i+1/2} = k_g s^g (a + \gamma x_{i+1/2})^p \tag{34}$$

This scheme displays first-order accuracy. For numerical flux reconstruction using the above equations, one upwind cell is evaluated at each time step for the convective flux (Eq. (33)). Treatment of the cells at the domain boundaries was described in the previous section. The upwind scheme is independent of the grid structure and does not require adjustment when extending from a uniform grid to a nonuniform grid.

4.2. High-resolution scheme by Koren

We also implemented and tested a representative high-resolution (HR) scheme developed by Barry (1993). There are other HR schemes available, including a very popular second order high-resolution scheme tested by Gunawan et al. (2004) that was based on LeVeque's analysis of hyperbolic equations (LeVeque, 2002). This popular scheme resembles an upwind flux plus a diffusive flux that is purposely chosen to exactly match the second term of the Taylor expansion of the growth term using a central finite difference method. Unfortunately, we could not implement this scheme in CADET because the diffusive flux term requires a fixed step size in time, which is incompatible with the adjustable time step size used in the BDF time integrator. The Koren HR scheme is also second-order accurate but does not require fixed time step sizes, making it compatible with CADET.

According to Koren's HR scheme (Barry, 1993), the convective flux on a uniform grid ($\Delta x_i = \Delta x$) reads as

$$\tilde{F}_{i+1/2} = \tilde{F}_{HR,i+1/2} = v_{G,i+1/2} \left(n_i + \frac{1}{2} \Phi_{i+1/2} (n_{i+1} - n_i) \right), \tag{35}$$

where $\Phi_{i+1/2}$ is the van Leer flux limiting function and $v_{G,i+1/2}$ is given by Eq. (34). This scheme originated in van Leer's κ zerowise Legendre polynomial interpolation applied to the cell average n_i where κ is a parameter that can be chosen to give purely linear ($\kappa = 0$) or quadratic ($\kappa = 1/3$) interpolation (van Leer, 1985). Koren showed that van Leer's original $\kappa = 1/3$ scheme was equivalent to Eq. (35) with

$$\Phi_{i+1/2} = \Phi_{ori,i+1/2} = \frac{1}{3} + \frac{2}{3} r_{i+1/2}, \qquad r_{i+1/2} = \frac{n_i - n_{i-1}}{n_{i+1} - n_i}$$

This scheme is globally a formal second order scheme with no flux limiting. Following Sweby's monotonicity theory, the scheme becomes *total variation diminishing* (TVD) by limiting the flux to satisfy the corresponding TVD properties. Various limiting functions have been proposed such as the van Leer, Superbee and minmod etc., but the van

Leer flux limiting function used in this study was chosen on the basis of preliminary studies by other authors who reported good results with this limiter (Gunawan et al., 2004; Qamar et al., 2009, 2006; Kumar et al., 2008). The van Leer flux limiter is defined as

$$\Phi_{i+1/2} = \frac{r_{i+1/2} + |r_{i+1/2}|}{1 + |r_{i+1/2}|}, \qquad r_{i+1/2} = \frac{n_i - n_{i-1} + \varepsilon}{n_{i+1} - n_i + \varepsilon}. \tag{36}$$

Here, $r_{i+1/2}$ is a local smoothness monitor for the cell face $x_{i+1/2}$ and $\varepsilon > 0$ is a small number used to avoid division by zero when the solution is smooth. The van Leer flux limiter $\Phi_{i+1/2}$ uses the monitor function $r_{i+1/2}$ to detect the smoothness near the cell face $x_{i+1/2}$ by evaluating the ratio of upwind and downwind slopes. For $r_{i+1/2} < 0$, the slopes have opposing signs, i.e. a local extremum is detected and the scheme is locally reduced to a first order upwind flux (i.e. $\Phi = 0$) to remain TVD. When $0 < r_{i+1/2} < 1$, the approximated function in the downwind region is smoother than in the upwind region and vice versa for $1 < r_{i+1/2} < 2$. Here, the limiting function yields a weighted flux reconstruction to stay within the TVD boundaries. If the local slope is constant, i.e. $r_{i+1/2} = 1$, the scheme becomes an unlimited 2nd order central difference scheme. Overall, the limiter avoids spurious oscillations by balancing the cell face flux approximation between a first order accurate and a second order accurate scheme depending on the smoothness of the solution.

The van Leer flux limiter evaluates two upwind cells and one downwind cell for each flux at each time step. For the cells at the domain boundaries, the flux needs to be reconstructed differently. The fluxes $F_{1/2}$ and $F_{N_x+1/2}$ are defined by the corresponding boundary conditions, as described in Section 3, while an upwind scheme (Eq. (33)) is used for $F_{1/2}$.

It is important to note that the algorithms presented above are only applicable on uniform grids. On nonuniform grids, unintended limiting could reduce the overall accuracy of the HR scheme. Consider a linear solution with slope s and a nonuniform grid with a stretching ratio of $a = 3/2$ such that $x_{i+1/2} - x_{i-1/2} = a(x_{i-1/2} - x_{i-3/2})$. The van Leer smoothness monitor becomes: $r_{i+1/2} = (n_i - n_{i-1} + \varepsilon)/(n_{i+1} - n_i + \varepsilon) = (s \cdot (x_{i-1/2} - x_{i-3/2}))/(s \cdot (x_{i+1/2} - x_{i-1/2})) = 1/a = 2/3$. The van Leer flux limiter results in $\Phi = 0.8$, sharpening the solution despite the fact that no limiting is required.

To address this issue, we implement and test a modified van Leer flux limiter proposed by Hou et al. (2012):

$$\begin{aligned} \Phi_{M,i+1/2} &= \frac{\frac{1}{2} R_{i+1/2} r_{M,i+1/2} + \frac{1}{2} R_{i+1/2} |r_{M,i+1/2}|}{R_{i+1/2} + r_{M,i+1/2} - 1} \\ r_{M,i+1/2} &= \frac{n_i - n_{i-1} + \varepsilon}{n_{i+1} - n_i + \varepsilon} \cdot \frac{\Delta x_{i+1} + \Delta x_i}{\Delta x_i + \Delta x_{i-1}}, \quad R_{i+1/2} = \frac{\Delta x_{i+1} + \Delta x_i}{\Delta x_i} \end{aligned} \tag{37}$$

and the flux on a nonuniform grid is updated to

$$\tilde{F}_{i+1/2} = \tilde{F}_{HRM,i+1/2} = \upsilon_{G,i+1/2} \left(n_i + \frac{\Phi_{M,i+1/2}}{R_{i+1/2}} (n_{i+1} - n_i) \right) \tag{38}$$

This modification is based on the use of scaling factors to adjust the smoothness monitor and limiting function. On a uniform grid, the modified van Leer flux limiter coincides with the unmodified form.

4.3. Weighted essentially non-oscillatory scheme

The weighted essentially non-oscillatory (WENO) reconstruction scheme avoids the use of flux limiters. It was first proposed by Liu et al. (1994) as an improvement of the ENO scheme developed by Harten et al. (1987), and then further improved by Jiang and Shu (1996). The underlying idea of the WENO scheme is to use a convex combination of lower order approximations based on r stencils $\{x_{i-r+1}, \ldots, x_{i+r-1}\}$ with each assigned a weight to achieve $(2r-1)$th order accuracy in smooth regions. The numerical flux is given by:

$$\tilde{F}_{i+1/2} = \tilde{F}_{WENO(2r-1),i+1/2} = \upsilon_{G,i+1/2} \sum_{m=0}^{r-1} W_m q_m^{(r)} \tag{39}$$

where $\upsilon_{G,i+1/2}$ is defined in Eq. (34), W_m and $q_m^{(r)}$ are the weights and polynomials for the mth stencil, respectively.

The weights are chosen in such a way that 1. near a discontinuity it is essentially zero to avoid using that stencil; 2. it is a smooth function of the cell averages involved and 3. the weights are computationally efficient. According to Shu (1998), weights that satisfy the above requirements are given by

$$W_m = \frac{\alpha_m}{\sum_{k=0}^{r-1} \alpha_k}. \tag{40}$$

The weighting parameter α_m depends on a smoothness indicator $IS_m^{(r)}$:

$$\alpha_m = \frac{C_m^{(r)}}{\left(IS_m^{(r)} + \varepsilon \right)^p}, \tag{41}$$

where $p = 2$ as suggested by Jiang and Shu (1996). The parameter $\varepsilon > 0$ is a small quantity originally introduced to avoid division by zero, but was later shown to impact the convergence order (Cravero and Semplice, 2016; Aràndiga et al., 2011). We implemented a grid-dependent $\varepsilon = \Delta x_i$ as suggested by Cravero and Semplice (2016). This choice was shown by Cravero and Semplice (2016) to preserve the convergence rate while providing better shock-capturing capability compared with a constant ε.

The coefficients C_m are chosen such that $(2r-1)$th order accuracy is achieved in smooth regions as expressed by the identity

$$q_{r-1}^{(2r-1)} = \sum_{m=0}^{r-1} C_m^{(r)} q_m^{(r)},$$

where $\sum_{m=0}^{r-1} C_m^{(r)} = 1$.

Lastly, the smoothness indicators are designed to be a measure of the total variation of the reconstruction polynomials inside each stencil:

$$IS_m^{(r)} = \sum_{k=1}^{r-1} \left(\Delta x_i^{2k-1} \int_{x_{i-1/2}}^{x_{i+1/2}} \left(\frac{\partial^k n}{\partial^k x} \right)^2 \mathrm{d}x \right),$$

where $-1 < m < r$. These indicators are a sum of the squares of the scaled L2 norm for all derivatives of the interpolation polynomials.

On a uniform grid, all coefficients are constant, which greatly simplifies the algorithm. We are mainly interested in the cases where $r = 2$ and $r = 3$. Denoting $q_m^{(r)}$ and $C_m^{(r)}$ evaluated at $x_{i+1/2}$ as $q_m^{(r-)}$ and $C_m^{(r-)}$, the polynomials $q_m^{(r)}$ read

$$\begin{gathered} q_0^{(2-)} = \frac{1}{2} n_i + \frac{1}{2} n_{i+1}, \quad q_1^{(2-)} = -\frac{1}{2} n_{i-1} + \frac{3}{2} n_i; \\ q_0^{(3-)} = \frac{1}{3} n_i + \frac{5}{6} n_{i+1} - \frac{1}{6} n_{i+2}, \; q_1^{(3-)} = -\frac{1}{6} n_{i-1} + \frac{5}{6} n_i + \frac{1}{3} n_{i+1}, \\ q_2^{(3-)} = \frac{1}{3} n_{i-2} - \frac{7}{6} n_{i-1} + \frac{11}{6} n_i. \end{gathered} \tag{42}$$

The parameters $C_m^{(r)}$ are given by

$$\begin{gathered} C_0^{(2-)} = 2/3, C_1^{(2-)} = 1/3, \\ C_0^{(3-)} = 3/10, C_1^{(3-)} = 6/10, C_2^{(3-)} = 1/10. \end{gathered} \tag{43}$$

The smoothness indicators $IS_m^{(r)}$ are given by

$$\begin{gathered} IS_0^{(2)} = (n_{i+1} - n_i)^2, \quad IS_1^{(2)} = (n_i - n_{i-1})^2, \\ IS_0^{(3)} = \frac{13}{12}(n_i - 2n_{i+1} + n_{i+2})^2 + \frac{1}{4}(3n_i - 4n_{i+1} + n_{i+2})^2, \\ IS_1^{(3)} = \frac{13}{12}(n_{i-1} - 2n_i + n_{i+1})^2 + \frac{1}{4}(n_{i-1} - n_{i+1})^2, \\ IS_2^{(3)} = \frac{13}{12}(n_{i-2} - 2n_{i-1} + n_i)^2 + \frac{1}{4}(n_{i-2} - 4n_{i-1} + 3n_i)^2. \end{gathered} \tag{44}$$

WENO23 ($r = 2$) evaluates two upwind and one downwind cells, while WENO35 ($r = 3$) evaluates three upwind and two downwind cells. For WENO23, an upwind scheme is applied to $\tilde{F}_{1/2}$. For WENO35, WENO23 is applied to $\tilde{F}_{3/2}$ and $\tilde{F}_{N_x-3/2}$ while an upwind scheme is applied to $\tilde{F}_{1/2}$.

On a nonuniform grid, all coefficients are dependent on the grid structure. For the cases $r = 2$ and $r = 3$, Smit et al. (2005) reported their explicit formula as a function of the grid structure. We have simplified the equations and summarized them below. The polynomials $q_m^{(r)}$, optimal weights $C_m^{(r)}$ and the smoothness indicators $IS_m^{(r)}$ evaluated at $x_{i+1/2}$ for WENO23 are given by

$$\begin{aligned} q_0^{(2-)} &= \frac{\Delta x_{i+1}}{\Delta x_i + \Delta x_{i+1}} n_i + \frac{\Delta x_i}{\Delta x_i + \Delta x_{i+1}} n_{i+1}, \\ q_1^{(2-)} &= (1 + \frac{\Delta x_i}{\Delta x_{i-1} + \Delta x_i}) n_i - \frac{\Delta x_i}{\Delta x_{i-1} + \Delta x_i} n_{i-1}, \\ C_0^{(2-)} &= \frac{\Delta x_{i-1} + \Delta x_i}{\Delta x_{i-1} + \Delta x_i + \Delta x_{i+1}}, C_1^{(2-)} = \frac{\Delta x_{i+1}}{\Delta x_{i-1} + \Delta x_i + \Delta x_{i+1}}, \\ IS_0^{(2)} &= (\frac{2\Delta x_i}{\Delta x_i + \Delta x_{i+1}})^2 (n_{i+1} - n_i)^2, \\ IS_1^{(2)} &= (\frac{2\Delta x_i}{\Delta x_{i-1} + \Delta x_i})^2 (n_i - n_{i-1})^2. \end{aligned} \tag{45}$$

The symbolic expressions for $q_0^{(3-)}, q_1^{(3-)}, q_2^{(3-)}, C_0^{(3-)}, C_1^{(3-)}, C_2^{(3-)}$, $IS_0^{(3)}, IS_1^{(3)}$ and $IS_2^{(3)}$ corresponding to the WENO35 scheme on a nonuniform grid are rather complicated despite our simplifications. For conciseness, they are reported in the SI.

5. Time integrator

After the discretization in space, we obtain an initial value problem (IVP) for a large system of ODEs that is solved in implicit form:

$$F(t, y, \dot{y}) = 0, \ y(0) = y_0, \ \dot{y}(0) = \dot{y}_0,$$

where y is the state vector, $\dot{y} = dy/dt$; the initial values of y_0 and $\dot{y}_0$ must be consistent. The resulting ODE system can be a stiff system for three main reasons. First, the nucleation term can lead to a sharp front in the solution which is hard for the time integrator to resolve. Second, the growth rate may be highly nonlinear when size-dependent growth mechanisms are considered. Third, the dispersive second order term can also cause stiffness. When using explicit ODE routines, the time step size must be carefully chosen to ensure stability (and hence convergence). For stiff problems, explicit time steps sizes are typically limited by stability constraints rather than accuracy, which significantly increases computational demands. To avoid this problem, we integrate the system in time using an implicit variable-step/variable-order backward differential formula (BDF)

$$\dot{y}(t_\tau) = \frac{1}{\Delta t_\tau} \sum_{i=0}^{q_\tau} \alpha_{\tau,i} y(t_{\tau-i}),$$

where q_τ is the order, t_τ is the time at step $\tau = 1, 2, \dots$, and Δt_τ is the time step size. Step size and order are adaptively changed, with the order ranging from one to five. The coefficient $\alpha_{\tau,i}$ is uniquely determined from the history of step sizes and order. The BDF is implemented in the implicit differential–algebraic solver (IDA) package in the suite of non-linear and differential–algebraic equation solvers (SUNDIALS) (Woodward and Balos, 2021). It is a robust and efficient time integrator designed for large, stiff ODE systems.

Application of the BDF to the IVP gives a nonlinear algebraic equation that needs to be solved at each time step τ:

$$G(y_\tau) = F\left(t_\tau, y_\tau, \frac{1}{\Delta t_\tau} \sum_{i=0}^{q_\tau} \alpha_{\tau,i} y(t_{\tau-i})\right) = 0. \tag{46}$$

By default, IDA uses Newton iteration to solve this equation. During each Newton iteration, the solution of a linear system is required

$$\mathbb{J}(y_\tau^{m+1} - y_\tau^m) = -G(y_\tau^m), \tag{47}$$

where y_τ^m is the mth approximation to y_τ, G is a vector-valued residual and $\mathbb{J}$ is an approximation of the system Jacobian

$$\mathbb{J} \approx \frac{\partial G}{\partial y} = \frac{\partial F}{\partial y} + \frac{\alpha_{\tau,0}}{\Delta t_\tau} \frac{\partial F}{\partial \dot{y}}.$$

Most of the runtime is consumed when solving Eqs. (46) and (47) repeatedly. One of the most burdensome tasks is the generation of the Jacobian. CADET can use automatic differentiation (AD) in forward mode as implemented in a previous release to generate the Jacobian: the computation of the Jacobian matrix with respect to the vector that contains the state variables y is broken down into a sequence of elementary arithmetic operations and elementary functions which can be automatically calculated based on the chain rule. However, computing the Jacobian using the chain rule repeatedly and storing and accessing it in the computer memory requires computational effort that inevitably slows down the simulations. To reduce the runtime, we supplement the solver with an analytical Jacobian:

$$\mathbb{J} = \begin{bmatrix} \frac{\partial G_c}{\partial c} & \frac{\partial G_c}{\partial n_1} & \dots & \frac{\partial G_c}{\partial n_{N_x}} & \frac{\partial G_c}{\partial c_{eq}} \\ \frac{\partial G_1}{\partial c} & \frac{\partial G_1}{\partial n_1} & \dots & \frac{\partial G_1}{\partial n_{N_x}} & \frac{\partial G_1}{\partial c_{eq}} \\ \vdots & & \ddots & & \vdots \\ \vdots & & \ddots & & \vdots \\ \frac{\partial G_{N_x}}{\partial c} & \frac{\partial G_{N_x}}{\partial n_1} & \dots & \frac{\partial G_{N_x}}{\partial n_{N_x}} & \frac{\partial G_{N_x}}{\partial c_{eq}} \\ \frac{\partial G_{c_{eq}}}{\partial c} & \frac{\partial G_{c_{eq}}}{\partial n_1} & \dots & \frac{\partial G_{c_{eq}}}{\partial n_{N_x}} & \frac{\partial G_{c_{eq}}}{\partial c_{eq}} \end{bmatrix}, \tag{48}$$

where G_c is the residual for the mass balance, G_i, $i \in \{1, \dots, N_x\}$, is the residual for n_i and $G_{c_{eq}}$ is the residual for the solubility pseudo-component. The symbolic expressions for the Jacobian are dependent on the schemes and are complicated. For conciseness, they are given in the SI. The correctness of the analytical Jacobian was checked by comparing it against a Jacobian matrix obtained by AD (Püttmann et al., 2016).

6. Implementation and numerical experiments

The discretized 1D and 2D governing equations are implemented and solved in the modular, free and open-source process modeling software package CADET (von Lieres and Andersson, 2010; Leweke and von Lieres, 2018). CADET supports several platforms, including Windows, Linux, and Mac OS. The numerical core is written in C++ and provides a Python interface and frontend. CADET was originally developed as a fast and accurate numerical solver for mechanistic modeling in chromatography, including consistent initialization. In recent years, it has been actively developed and extended to tackle numerical challenges in other fields. Implementation of the PBM in CADET has several advantages: 1. CADET supports mathematical models and dedicated solvers for other important unit operations, including chromatography and filtration. The implemented model family also covers valves, switches, and tubes to model effects that are external to the reactor (or column). The output of the PBM can be directly linked to these units for integrated simulations of processes that consist of multiple unit operations; 2. Existing infrastructure was reused to allow, for example, efficient computation of parameter sensitivities via AD (Püttmann et al., 2013). The Python frontend provides a variety of tools to solve typical engineering tasks, such as model calibration, process optimization, and uncertainty quantification. 3. By making the methods and results of this work publicly available in a continuously developed and maintained open-source software, it becomes a lasting contribution.

The implementation of the previously introduced algorithms is validated using seven test cases. Approximation error and solver efficiency are analyzed and benchmarked for all these cases. Analytical solutions were used when available. Otherwise, numerical solutions on fine grids were used as reference solutions. For nonuniform grids, the intermediate points of the distribution are interpolated using univariate splines. All tests and benchmarks are performed on a 3600 MHz AMD Ryzen(TM) Threadripper(TM) with 32 cores and 64 threads. Unless otherwise specified in the test cases, analytical Jacobians are used and

IDA is configured so that the initial time step size is 10^{-6}, the relative tolerance is 10^{-7}, and the absolute tolerance is 10^{-7}.

We calculate the normalized L1 norm to measure the difference between two solutions:

$$\|f\|_{L^1} = \frac{\sum_{i=1}^{N_x} \Delta x_i |n_i^{\text{(numerical)}} - n_i^{\text{(reference)}}|}{\sum_{i=1}^{N_x} \Delta x_i n_i^{\text{(reference)}}}. \tag{49}$$

The experimental order (rate) of convergence based on L1 norm for the internal coordinate x is calculated using

$$\text{EOC}_{L^1} = log_{N_x^{(\text{B})}/N_x^{(\text{A})}} \left(\frac{\|f\|_{L^1}^{(\text{A})}}{\|f\|_{L^1}^{(\text{B})}} \right) \tag{50}$$

where A and B represent two independent simulations and N_x is the total number of cells for the particle space. We also analyze the quality of the numerical solution by comparing the moments of the distributions. The discrete pth moment M_p is given by

$$M_p = \sum_{i=0}^{N_x} x_i^p n_i \Delta x_i. \tag{51}$$

The volume fraction is defined as $V_i = n_i x_i^3 \Delta x_i / M_3$.

The test cases are organized as follows: cases 1 to 5 demonstrate the successful implementation of one of the terms of the 1D- or 2D-PBM decoupled from the mass balance equation. Cases 6 and 7 address the 1D- or 2D-PBM coupled to the mass balance equation. Model parameter values used in these tests are reported in the SI.

6.1. *Case 1: size-independent growth*

In this test, we validate our 1D PBM implementation with a size-independent growth term and compare the effectiveness of the upwind, HR Koren, and WENO schemes. This test was also used by Motz et al. (2002) and Qamar et al. (2006). Consider a simple population balance equation for a BSTR:

$$\frac{\partial n}{\partial t} = -v_G \frac{\partial n}{\partial x}$$

with boundary condition $n(0,t) = 0$ and initial distribution:

$$n(x,0) = n_0(x) = \begin{cases} 10^{10} & \text{for } 10 < x < 20, \\ 0 & \text{otherwise.} \end{cases}$$

This case has the analytical solution $n(x,t) = n_0(x - v_G t)$: the initial particle size distribution travels along the positive direction of the x coordinate with rate v_G. Due to absence of nucleation and size-independent growth processes, the size and shape of the distribution remain constant. Because the mass balance is not considered, the particles grow in size indefinitely.

Two initial distributions were considered: the first has a rectangular shape with discontinuities. This provides a rigorous test for numerical schemes and their implementation: the peak is sharp and the growth rate is high, which together pose a challenge to the shock-capturing capabilities of the schemes. The results are shown in Fig. 2. At $t = 10$ s, all schemes captured the sharp fronts relatively well. However, as time increased to $t = 50$ s, the solutions of all schemes spread out as a result of the numerical dispersion. As expected, the upwind scheme exhibited the largest numerical dispersion when using the same number of cells N_x. The HR scheme performed better in capturing the sharpness. WENO23 spread out more than the HR scheme but performed much better than the upwind scheme. WENO35 outperformed all other schemes but introduced minor overshoots. To quantitatively study the differences between these schemes, further analyses on the convergence rate and runtime were carried out. Fig. 2(b) shows the normalized L1 norm as a function of the number of cells where the slope in the log–log plot represents the rate (order) of convergence. All schemes exhibited a first order convergence rate. Note that the rates of all the high-order schemes were below their designed rates. This is expected as the designed rate can only be achieved for smooth solutions. However, WENO35 reached the highest convergence rate (0.8) and the smallest error given the same number of cells. Fig. 2(c) reports the normalized L1 norm versus runtime. Minimizing both error and runtime results in a Pareto problem: points that are closest to the origin (0,0) are Pareto optimal, and indicate the best algorithm to most efficiently achieve the respective accuracy. For Pareto optimal points, one objective can only be improved by impairing the other. All other points are dominated by the Pareto front. In this case, the WENO35 scheme was obviously Pareto optimal since it could achieve the smallest error for any given runtime in the tested ranges.

The second initial distribution tested was a log-normal distribution:

$$n_0 = y_0 + \frac{A}{\sqrt{2\pi} w x} e^{\frac{-\left(\ln \frac{x}{x_{ce}}\right)^2}{2w^2}}, \tag{52}$$

where $y_0 = 0$ is the offset, $A = 10^{10}$ is the area, $w = 0.3$ is the width, and $x_{ce} = 20$ is the center of the seed distribution. Similar to the first distribution case, the higher-order schemes were superior to the upwind scheme as time elapsed from $t = 10$ s to $t = 50$ s. As shown in Fig. 2(d) and quantified in Fig. 2(e), high-order schemes approximated the analytical solution much better than the upwind scheme. Since the log-normal distribution is smooth, the experimental convergence rates of these schemes were much better than those for the discontinuous distribution: the HR Koren scheme reached its maximum designed rate of two, while the WENO23 and WENO35 rates were also within their theoretical ranges between 2 and 3, and between 3 and 5, respectively. The normalized L1 norm vs. runtime is reported in Fig. 2(f). Here, the WENO35 scheme was again the best choice, as it dominated all other schemes within the error range tested.

We further compare the performance of the schemes in terms of the resulting calculated moments of the PSD which are of important practical use: the moments allow the calculation of common scalar metrics of the distribution, such as the total particle count, the mean particle size, and the variance of the size distribution. In the above tests, all schemes experienced numerical dispersion to a certain degree, which also raised questions about the accuracy of the moments. In Fig. 3(a), we compared the simulated and analytical moments for the rectangular initial distribution case from the zeroth up to the sixth order. Since there is no nucleation source term in this test case, the total count of the particles is preserved and, hence, solely depends on the initial distribution. All schemes demonstrated an accurate prediction of the zeroth order moment, i.e., conservation of the total count of the particles. This is a conditio sine qua non because a correct implementation of the finite volume method must always preserve the zeroth order moment. However, the errors in other moments increased as the order increased with the largest error seen in the sixth order moment. The upwind scheme showed the highest relative error of around 20%. WENO23 was slightly inferior to the HR Koren scheme and WENO35 outperformed all other schemes with a maximum relative error of less than 2.5% for all moments. Overall, higher order schemes worked satisfactorily for all moments (relative error $\leq 5\%$) even when a modest number of cells was used.

6.2. *Case 2: size-dependent growth*

In this test case we validate our implementation of a size-dependent growth term for a BSTR model. This case was also used by Gunawan et al. (2004), Kumar and Ramkrishna (1997) and Qamar et al. (2006). Consider a simple population balance equation

$$\frac{\partial n}{\partial t} = -\frac{\partial (v_G n)}{\partial x}$$

with a growth rate that depends linearly on the particle size: $v_G = v_{G,0} x$. We assume that the initial distribution is given by $n(x,0) = N_0/\overline{L} \times \exp(-L/\overline{L})$, where N_0 is the total initial particle number of size $\overline{L}$ and $\overline{L}$ is the mean size of the distribution. This scenario

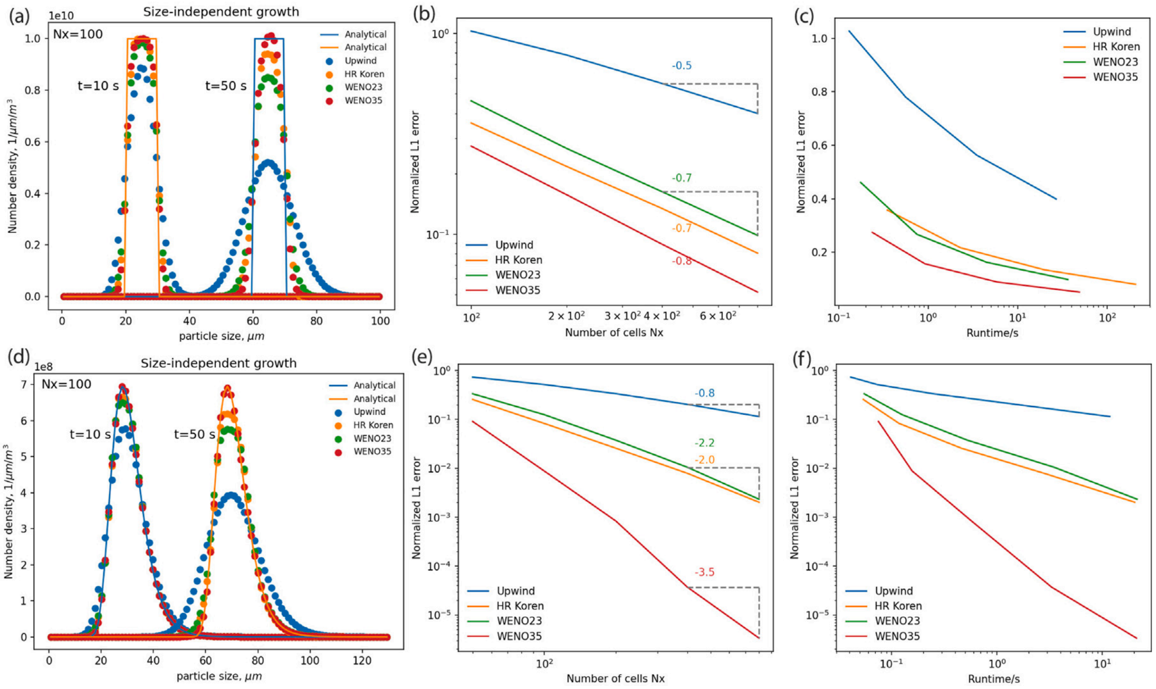

Fig. 2. Case 1: size-independent growth. Rectangular (top) and log-normal (bottom) initial distribution. (a), (d): numerical solutions and analytical references; (b), (e): normalized L1 norm vs. number of cells at $t = 50$ s; (c), (f): normalized L1 norm vs. runtime. AD was used in (c).

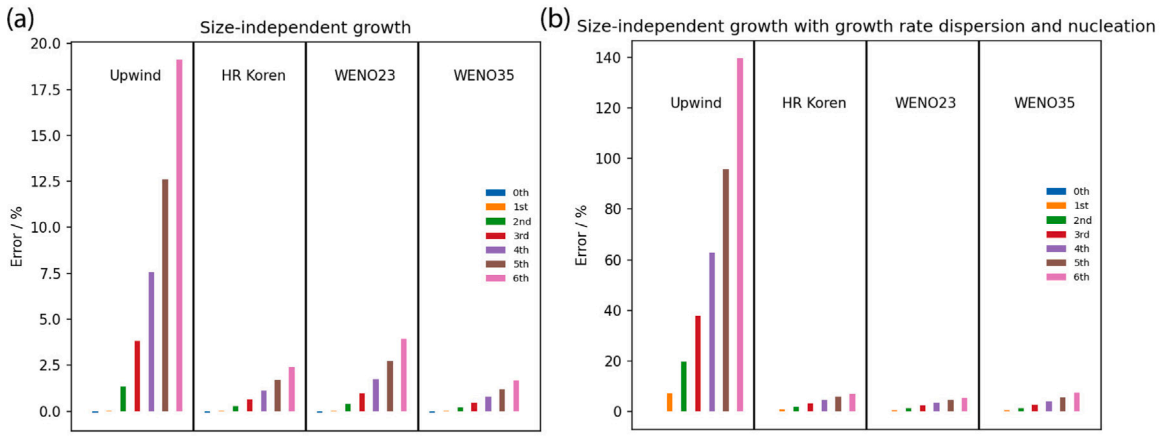

Fig. 3. Moment error analysis. $N_x = 100$ is fixed. (a): Case 1: rectangular initial distribution at $t = 50\,s$; (b): Case 4: $\mathrm{Pe}_G = 10$ and $t = 6$ s.

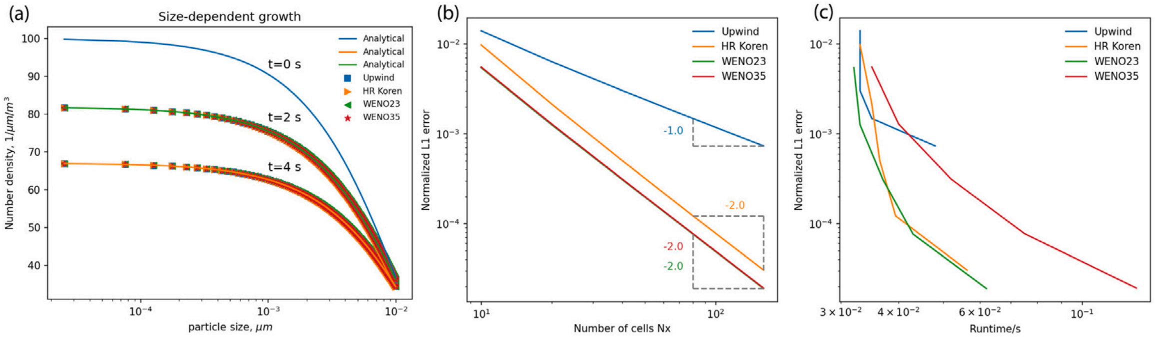

Fig. 4. Case 2: size-dependent growth. (a): numerical solution vs. analytical solution; (b): normalized L1 norm vs. number of cells N_x at $t = 4$ s; (c): normalized L1 norm vs. runtime.

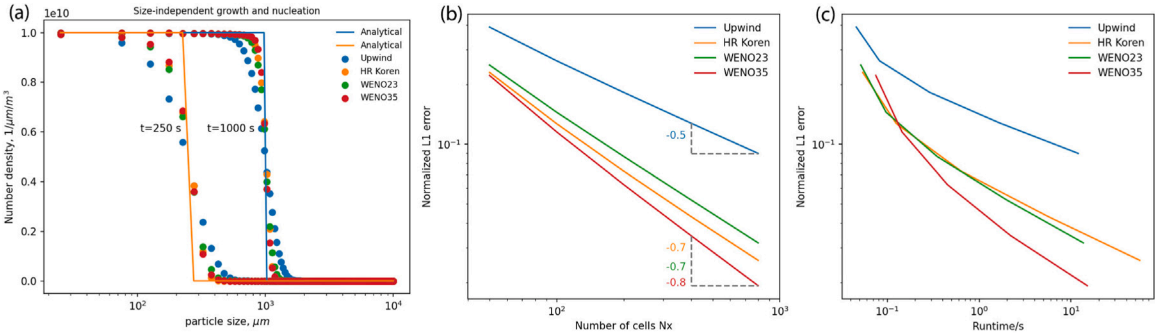

Fig. 5. Case 3: size-independent growth and nucleation. (a): numerical solution vs. analytical solution; (b): normalized L1 norm vs. number of cells N_x at $t = 1000$ s; (c): normalized L1 norm vs. runtime.

has an analytical solution (Kumar and Ramkrishna, 1997): $n(x,t) = \frac{N_0}{L} \exp\left[-\frac{x}{L} e^{-v_{G,0}t} - v_{G,0}t\right]$.

Fig. 4(a) shows that the results of all the numerical schemes implemented were in excellent agreement with the analytical solution at times $t = 2$ s and $t = 4$ s. Fig. 4(b) shows that the HR Koren and WENO schemes converged with a rate of 2. Although the HR Koren scheme had the same rate as the WENO schemes, it exhibited a higher normalized L1 norm for the same number of cells. Fig. 4(c) shows that the HR Koren and WENO23 schemes were almost equal in performance and both were Pareto optimal. The WENO35 scheme, despite having the same experimental rate and normalized L1 norm as the WENO23 scheme, exhibited an increased runtime caused by the higher computational effort required.

6.3. Case 3: size-independent growth with nucleation

In this case, we validate our implementation of the nucleation term when introduced as a point source in the 1D PBM for a BSTR. In this case, the PBM remains decoupled from the mass balance. This test was also used by Kumar and Ramkrishna (1997) and Kumar et al. (2008). Consider a population balance equation:

$$\frac{\partial n}{\partial t} = -v_G \frac{\partial n}{\partial x} + B_0 \sigma(x - x_c)$$

We assume the critical nuclei have negligible sizes ($x_c = 0$) and the balance equation has the initial and boundary conditions $n(x, 0) = n(0, t) = 0$. Hounslow (1990) has provided an analytical solution: $n = \frac{B_0}{G_0} H(t - \frac{x}{G_0})$, where G_0 is a constant and H is the Heaviside function. Since $B_0 = B_p + B_s$, we test the terms for both primary and secondary nucleation by setting $B_p = B_s = 5 \cdot 10^9$.

Fig. 5(a) shows the simulation results. The analytical solution has a rectangular shape because the particles are continuously nucleated with the same size and grow at a constant rate. The front has a true discontinuity as no particles larger than those growing from the nuclei nucleated at $t = 0$ s should exist. The upper constant value 10^{10} is the sum of B_p and B_s, indicating the correct implementation of both nucleation terms. Both terms were also tested independently with the same result (data not shown). Similar to case 1, all schemes were challenged to capture the discontinuity with the upwind scheme performing the worst and the WENO35 performing the best. The error was analyzed at $t = 1000$ s with results shown in Fig. 5(b). As expected, the experimental convergence rates for all schemes were below their designed rates. The WENO35 scheme performed better than all other schemes. The HR Koren and WENO23 schemes exhibited similar rates, but the HR Koren scheme had lower normalized L1 norms for a given N_x. Fig. 5(c) shows that the WENO35 scheme performed the best for errors below ca. 0.15, while HR Koren and WENO23 performed similarly for larger errors.

6.4. Case 4: size-independent growth, nucleation and growth rate dispersion

In this case, we validate our implementation of the growth rate dispersion term. An analytical solution of the governing equation for the given regularity boundary condition is not available. However, an analytical solution exists if we relax this boundary condition by assuming that the number density at infinite sizes is negligibly small. This assumption is valid if we choose x_{max} to be large enough. Even though theoretically nonzero, the continuous number density distribution rounds down to zero above a sufficiently large x_{max}, as real particles cannot become infinitely large. Consider a population balance equation for a BSTR, uncoupled from the mass balance,

$$\frac{\partial n}{\partial t} = -v_G \frac{\partial n}{\partial x} + D_g \frac{\partial^2 n}{\partial x^2}.$$

We assume $x_c = 0$ and that v_G is a constant, introduce the nucleation term B_0 as a boundary condition, and modify the regularity boundary condition:

$$n(x,0) = 0, \quad \left(n v_G - D_g \frac{\partial n}{\partial x}\right)|_{x=0} = B_0 = v_G n_0, \quad \frac{\partial n}{\partial x}|_{x \to \infty} = 0,$$

where the last equation is a simplification of the original regularity boundary condition by assuming $n(x \to \infty) = 0$, which will be examined by inspecting the last cell. An analytical solution was provided by Mason and Weaver (1924) and Gershon and Nir (1969) and could be found in the SI.

The largest size considered is set to $x_{max} = 500$ μm in the simulations to ensure that n in the last cell is negligible. Fig. 6 shows the analytical and simulated results for $x \in [0, 150]$. The largest value of n in the last cell for all the tested parameter sets were found to be $4.9 \cdot 10^{-42}$ ($N_x = 100$), which is negligible compared with the starting value of 0.10, justifying our simplification of the regularity boundary condition. Compared with the sharp decrease in the analytical solution in the previous test case, the spread in the distribution is a result of the growth rate dispersion. The larger the growth rate dispersion coefficient, the more spread out the solution becomes.

We can define a growth Peclet number Pe_G as

$$\mathrm{Pe}_G = \frac{v_G \overline{L}}{D_g}.$$

Typical growth Peclet numbers are reported to range from 5 to 10 (Randolph and White, 1977) with both ends of the range considered in this test. For a given Peclet number, D_g depends on the mean size of the PSD, which cannot be determined with an unknown D_g. This circular dependency is resolved by fixed-point iteration: starting with an initial guess for D_g, the mean size is calculated from the simulated PSD of interest. Then D_g is updated using this mean size, and the procedure is repeated until D_g converges.

The lower bound test has a relatively small growth Peclet number of $\mathrm{Pe}_G = 5$, indicating a strong growth rate dispersion. The upper

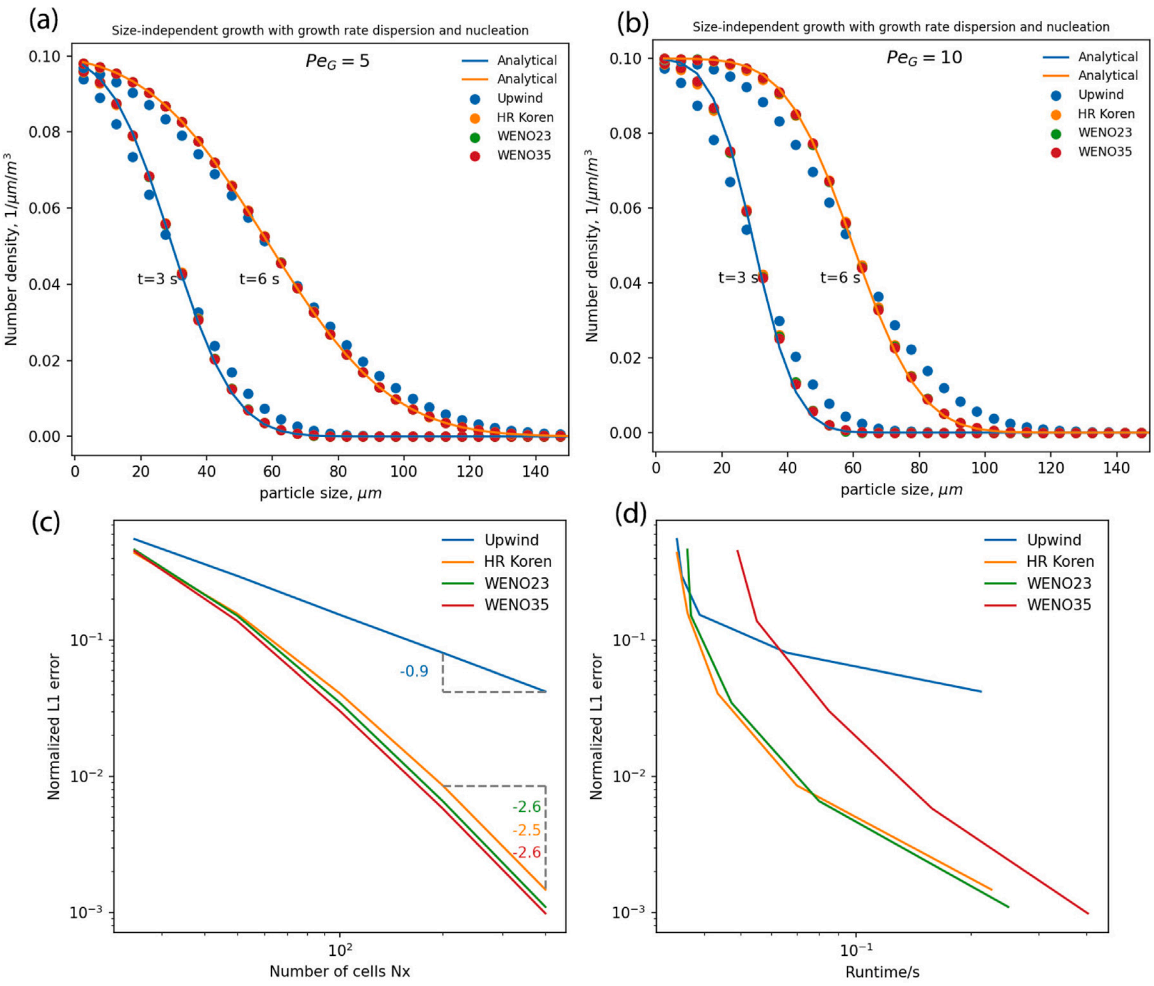

Fig. 6. Case 4: size-independent growth with growth rate dispersion and nucleation. The bottom panel is based on the case where $\mathrm{Pe}_G = 10$ and $t = 3$ s.

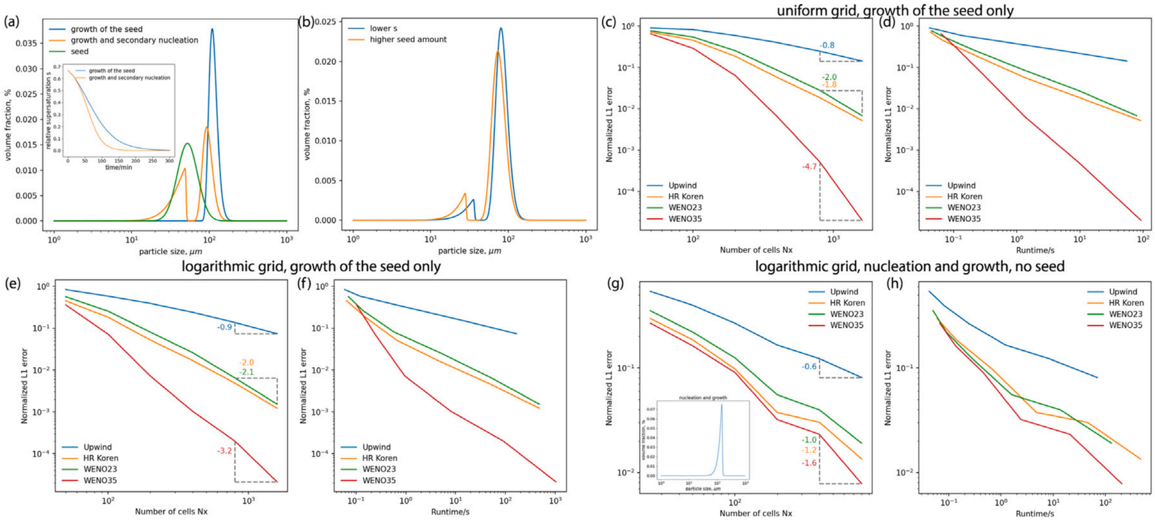

Fig. 7. Case 5: isothermal seeded crystallization in a BSTR.

bound test has a relatively large growth Peclet number of $\mathrm{Pe}_G = 10$, indicating weak growth rate dispersion. As can be seen in Fig. 6(a–b), the upwind scheme was more dispersive and deviated from the analytical solution more than the high-order schemes no matter which Pe_G and t was tested when using the same number of cells. However, when Pe_G decreased, the upwind scheme demonstrated improved performance because the stronger numerical dispersion inherent to the upwind scheme reconciled with the actual modeled dispersion.

The error and convergence rate analysis agreed with the above observation and showed that the upwind scheme demonstrated the largest normalized L1 norm followed by HR Koren, WENO23 and then WENO35 for the same N_x. Except for the upwind scheme, a similar convergence rate of around 2.6 was observed for all high-order schemes. While the experimental rates for the upwind and WENO23 were easy to explain, the rates for HR Koren and WENO35 were not within their expected ranges and required further elaboration. There are several convoluted factors contributing to this observation. First, for finite volume methods, the convergence rate of the high-order schemes for the growth flux reconstruction cannot exceed the order of the boundary treatments. As mentioned in Section 3, the rate of the high-order schemes were reduced as the lower boundary is approached, rendering an order of 1 for the first cell. Furthermore, the contribution of the first cell to the overall convergence rate when increasing N_x is also reduced, leading to an overall second-order boundary treatment. Second, the dispersion term was approximated using a second order approximation. Depending on how strong the growth dispersion is compared with the growth, the overall convergence rate may vary between 2 and the chosen order of the flux reconstruction for the growth which is again limited by the order of the boundary treatment. In this test, the expected convergence rate for all high-order schemes is 2. However, an even better convergence rate of about 2.6 was observed for the high-order schemes implemented. This indicates that the high-order schemes were correctly implemented as the design-order discretization-error convergence is an asymptotic property and represents a lower bound. Further, the same convergence rate (about 2.4) for the WENO schemes had also been observed in our previous work (Leweke and von Lieres, 2018). As seen in Fig. 6(d), the WENO35 scheme not only could not reach its optimal rate due to the limitations of the boundary treatment, but also involved more computations which increased its runtime, making HR Koren and WENO23 the best schemes for this test case.

A moment analysis was also performed for the case where $\mathrm{Pe}_G = 10$ and $t = 6$ s. To obtain the analytical moments, direct integration of the analytical solution is difficult. Instead, we used Simpson's rule on a fine grid (10,000 points between 0 and 150) to obtain highly accurate reference values. The relative percent error is presented in Fig. 3(b). As expected, the zeroth order moment is always accurate, indicating a correct implementation. The upwind scheme showed the largest relative error for the sixth order moment, with errors as high as 140%. Overall, high-order schemes worked satisfactorily in capturing these moments and increased accuracy can be achieved by increasing N_x at the cost of runtime.

6.5. Case 5: isothermal seeded crystallization in a BSTR

In this case, the PBM (Eq. (2)) is coupled to the solute mass balance equation (Eq. (8)). We assume that the seed distribution is characterized by a log-normal distribution (52) with $y_0 = 0$, $A = 10^{15}$, $w = 0.3$ and $x_{ce} = 40$. Unfortunately, an analytical solution is not available when the mass balance equation is considered. Instead, reference solutions were obtained using the WENO35 scheme on a fine logarithmic grid.

Fig. 7(a) shows the results. The green curve is the seed distribution. The blue curve is the simulated results for an ideal case assuming that the experimental conditions are carefully designed such that the particles only grow on the seed and no secondary nucleation occurs. A unimodal distribution was obtained. Compared with the seed distribution, the final PSD seemed to be narrower due to the scaling on the logarithmic grid. The orange curve represents a case where unwanted secondary nucleation occurs, which affects the growth of the seed. A bimodal distribution was observed as a result of both the growth of the seed particles and secondary nucleation. The sharp front of the first mode (counting from left to right) was the result of secondary nucleation, which decreased rapidly when supersaturation s decreased due to the solute mass consumed by nucleation and growth, leading to a classic tailing behavior. The second mode comes from the growth of the seed particles. Compared to the same mode in the growth-only case, there were significantly fewer large particles. This is not surprising since a fraction of the total solute mass was transferred to the first mode. The inset picture depicts the relative supersaturation s as a function of time: the initial relative supersaturation $s = 0.67$ gradually decreased to zero, which stopped further nucleation and growth. As expected, s decreased faster when secondary nucleation was considered.

If the first mode or the secondary particles are undesirable, increasing the amount of seed or using a lower supersaturation helps alleviate the problem. The blue curve in Fig. 7(b) shows the results obtained by decreasing the initial supersaturation ($s = 0.25$). Compared to the orange curve in (a), which had a supersaturation of $s = 0.67$, the height of the first mode was reduced by a factor of three. Similarly, when the initial seed amount was quadrupled, the first mode was also substantially reduced in population. In other words, a higher supersaturation or a lower seed amount induced a stronger or an early onset of secondary nucleation. This result agreed well with the experimental observations made by Caillet et al. (2007), Frawley et al. (2012) and Saleemi et al. (2012).

Further error analysis were thoroughly carried out for three different situations (cases 5A-C). Cases 5A-B considered the growth of the seed alone on different grid structures. Case 5C considered nucleation and growth on a logarithmic grid. In case 5 A (Fig. 7(c), (d)) where a uniform grid was used, the WENO35 performed much better than all other schemes, exhibiting a convergence rate of 4.7 compared with 0.8, 1.8 and 2.0 observed in the upwind, HR Koren and WENO23 scheme, respectively. The rates for all the high-order schemes were expected with the WENO35 approaching its upper bound and the WENO23 lying on its theoretical lower bound. Since the solution was not entirely smooth, the HR Koren scheme did not reach its maximum theoretical rate of 2.

In case 5B ((e), (f)), we are concerned with using a logarithmic grid structure as the PSD is often reported inherently on a logarithmic grid by the particle size distribution measurement instrument used. Compared to the uniform grid case, the experimental convergence rate for the WENO35 scheme decreased from 4.7 to 3.2, but was still within the expected range. In contrast, the rates for the upwind, HR Koren, and WENO23 schemes were slightly increased by about 0.1. Case 5C ((g), (h)) considered nucleation and growth alone without seeds. Compared with cases 5 A and B, the rates for all high-order schemes were dramatically decreased with a highest rate of 1.6 observed for the WENO35 scheme. This was expected as explained in Case 4. With cases 5A-C considered, the WENO35 scheme was the best scheme for this test case, since its performance always dominated the other schemes ((d), (f), (h)).

The convergence rates on nonuniform grids in this case were obviously inferior to those attained on uniform grids. This was not totally unexpected as similar results can be found in the literature. Central finite volume schemes are known to be only first-order accurate on logarithmic grids (Turkel, 1986). Wellner also reported a reduced experimental convergence rate for the WENO schemes on nonuniform grids for an entropy advection problem (Wellner, 2016). The deterioration might be attributed to the fact that the finite volume scheme is not generally consistent on nonuniform grids which can lead a reduction of the rate of discretization error (Diskin and Thomas, 2010; Svärd et al., 2008). However, a formal and rigorous analysis on the grid geometry's impact on the discretization error convergence rate for high-order schemes is beyond the scope of this article.

Regarding the runtime, there is one interesting note. The logarithmic grid posed a bigger numerical challenge: given the same N_x, all schemes had much longer runtimes compared to their uniform grid counterpart (Figure S1(a) and (b)). This is not surprising as the logarithmic grid has a higher cell density near the lower and middle

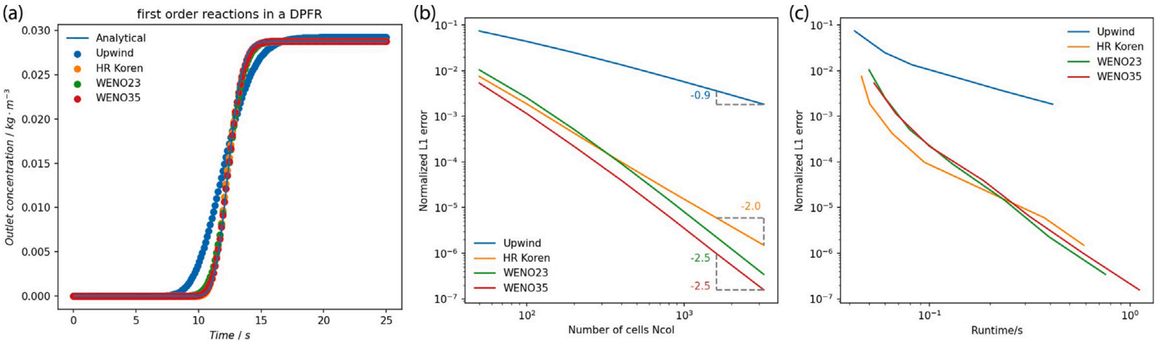

Fig. 8. Case 6: Solute transport in a DPFR with a first-order reaction.

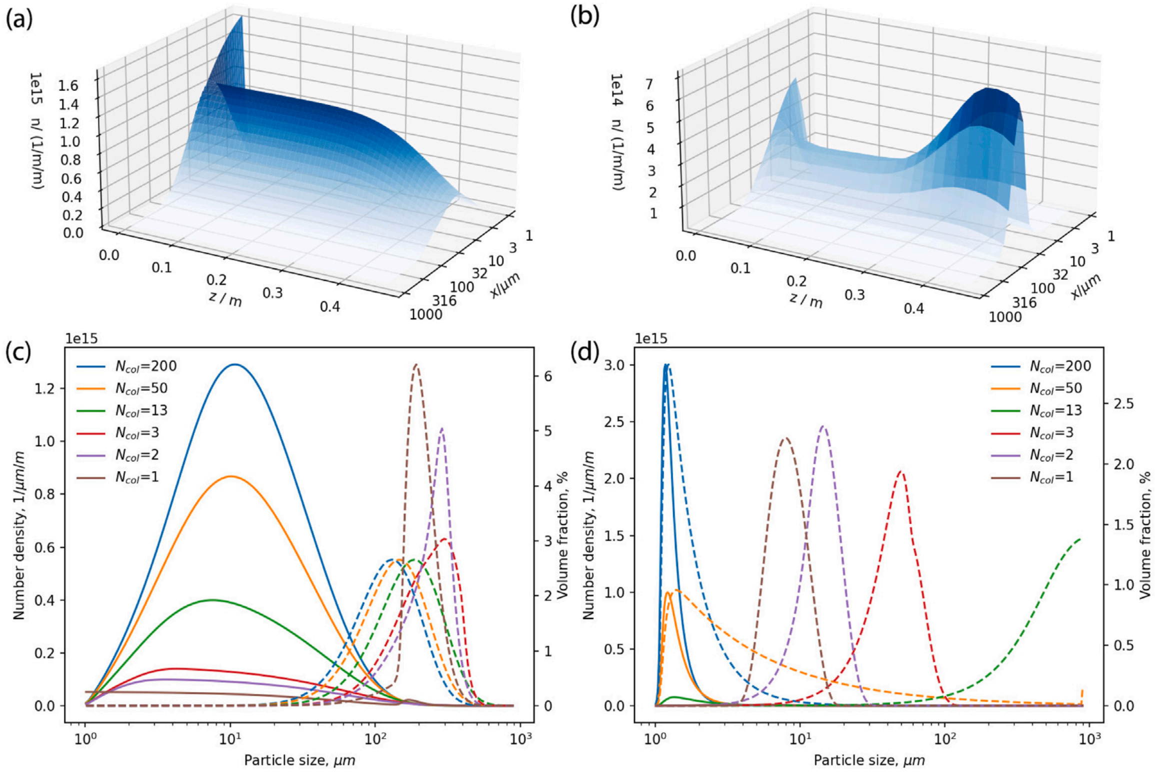

Fig. 9. The solid curves are the number density distributions and the dashed curves are the volume fraction distributions. (a), (b): PBM solutions in a DPFR. $N_x = N_{col} = 100$ with WENO35. Non-equilibrium solutions at $t = 80$ s. (a): case 7 A; (b): case 7B. (c) (d): flow equilibrium solutions at the reactor outlet ($t = 200$ s). (c): case 7 A, $N_x = 200$; (d): case 7B, $N_x = 400$.

parts of the size domain where the solution resides. It can be seen as a local grid refinement such that it better approximates the true solution but increases the runtime as a trade-off. Further, calculations of the high-order scheme coefficients are also more complicated on logarithmic grids.

6.6. Case 6: DPFR with a first-order reaction

The above five cases considered the internal coordinate x alone. The finite volume discretization of the external coordinate z using the upwind, WENO23 and WENO35 schemes were implemented in CADET and thoroughly validated and benchmarked in separate studies (von Lieres and Andersson, 2010; Leweke and von Lieres, 2018). As a new feature, the HR Koren scheme is implemented for the external coordinate in this article. To demonstrate its correct implementation and prepare the 2D-PBM case, we present a case study to recapitulate the key points for the external coordinate z alone by examining a first order reaction in a DPFR. The relative and absolute tolerances in this case were set to 10^{-11}.

Consider a one-dimensional convective-diffusive solute transport equation in the axial coordinate z with a first-order reaction sink term:

$$\frac{\partial c}{\partial t} = -v_{ax}\frac{\partial c}{\partial z} + D_{ax}\frac{\partial^2 c}{\partial z^2} - \mu c,$$

where μ is the first-order reaction forward rate constant. We assume the above equation is subject to the following Danckwerts boundary conditions and an initial condition with no solute:

$$c(z,0) = 0, \quad (v_{ax}c - D_{ax}\frac{\partial c}{\partial z})|_{z=0} = v_{ax}c_0, \quad \frac{\partial c}{\partial z}(L,t) = 0,$$

where c_0 is the solute feed concentration and L is the length of the reactor. The PDE admits an approximate analytical solution given by van Genuchten and Alves (1984) which can be found in the SI.

The solute concentration at the outlet of the DPFR is plotted as a function of time in Fig. 8(a). The feed concentration was $0.1\ \mathrm{kg/m^3}$ but the solute outlet concentration in flow equilibrium was less than

$0.03\ \mathrm{kg/m^3}$, reflecting the fact that the solute was partly consumed by the first-order reaction. Despite the small number of cells $N_{col} = 50$ we used in this test, the WENO23 and WENO35 schemes exhibited excellent agreement with the analytical solution. The upwind scheme, on the other hand, was again dispersive and showed minor over-predictions. Further error analysis showed error convergence rates of (0.9, 2.0, 2.5, 2.5) for the upwind, HR Koren, WENO23 and WENO35 schemes, respectively. Since the solute also entered the system through the left Danckwerts boundary condition, the WENO35 scheme did not reach a designed rate between 3 and 5, limited by the order of the boundary flux treatment. Interestingly, for a normalized error larger than about 10^{-4}, the HR Koren scheme exhibited a smaller error compared to the WENO23 scheme using the same number of cells N_{col}. However, it was surpassed by the WENO23 scheme for errors smaller than about 10^{-4}, due to the smaller convergence rate of the HR Koren scheme. Taking the runtime into account, as seen in Fig. 8(c), the HR Koren scheme was superior to other schemes for a normalized error larger than 10^{-5}, but was superseded by the WENO23 and WENO35 schemes in an even smaller error regime.

6.7. Case 7: isothermal continuous precipitation in a DPFR

In this case study we present a test corresponding to the isothermal continuous precipitation of a solute in a DPFR. The 2D governing equation (11) is coupled to the solute mass balance equation (15). The PSD distribution of interest is that obtained at the reactor outlet when flow equilibrium was achieved. Reference solutions were generated on a fine grid since there were no analytical solutions available for this case. Two situations were considered (cases 7A-B): case 7 A assumed that the particles were born as critical nuclei, and case 7B assumed that the particles were nucleated with an intrinsic log-normal distribution. Uniform and logarithmic grids for the internal particle coordinate x were tested for both cases. A uniform grid was consistently used for the external axial coordinate z. To reduce complexity, the same numerical scheme was used for the internal and external coordinates, even though other combinations are generally possible. There are two questions we want to answer: 1. what is the best scheme for both coordinates and; 2. what is the optimal trajectory to increase the cell number in both coordinates to stay on the Pareto fronts? This analysis includes the normalized L1 norm of the distribution itself and the percent errors of several scalar metrics. For each scheme in both cases 7A-B, 25 simulations with varying cell numbers in both coordinates were evaluated on a 5x5 grid. The exact grid arrangement can be found in Table S10 in the SI.

6.7.1. Case 7A: particles are born as critical nuclei

In case 7 A, particles are born as critical nuclei on a logarithmic grid. The full 2D-PBM solutions can be obtained at any discrete time point inside the reactor: Fig. 9(a) shows solutions at $t = 80$ s, when the flow has not yet reached equilibrium and a transient behavior was observed. The time required to reach flow equilibrium can be identified by a residence time study, and was found to be about 120 s. In practice, we are mainly interested in the flow equilibrium solutions at the reactor outlet, therefore, numerical solutions obtained at $t = 200$ s at the outlet were used for further analysis. When comparing numerical solutions obtained using different numbers of cells in the axial coordinate N_{col}, we noticed that a sufficiently large N_{col} was crucial for accurate approximations. In Fig. 9(c), an insufficient N_{col} led to a truncated intensity of the number density distribution and over-predictions of the amount of large particles. $N_{col} = 1$ and 2 also presented interesting special cases as the WENO35 scheme was not fully developed and reduced to the upwind scheme. These cases were essentially approximations of the DPFR by a single CSTR and two CSTRs in series, with both having large errors.

Fig. 10 shows the normalized L1 norm vs. runtime. Interpretation of this figure is similar to those in the 1D cases. However, in the 2D case each scheme has Pareto-optimal and dominated points, originating from different combinations of N_{col} and N_x. Pareto-optimal points within each scheme were connected by a line of the same color. The relative position of these lines determines the Pareto front across all schemes. In case 7 A, Fig. 10(a), all high-order schemes showed similar performance and were Pareto optimal.

Fig. 11(a) shows the normalized L1 norm vs. N_x and N_{col}. The surface gradients along the N_x direction were steeper than that in the N_{col} direction, indicating a faster decrease of the error when increasing N_{col} compared with increasing N_x. We observed that along the N_x axis, the gradient slope (rate) decreased as N_x increased. For instance, the slope along the N_x coordinate at a fixed $N_{col} = 600$ decreased from (1.2, 1.6, 1.9, 2.8) to (1.0, 0.7, 0.1, 0.4) for the upwind, HR Koren, WENO23 and WENO35 schemes, respectively. In contrast, the gradient slope along the N_{col} coordinate increased as N_{col} increased. For instance, the gradient slope along the N_{col} coordinate at a fixed $N_x = 200$ increased from (0.9, 0.9, 0.9) to (3.2, 3.5, 3.4) for the HR Koren, WENO23 and WENO35 schemes, respectively. These changes can be explained in the following way. The global normalized L1 norm for 2D case can be described by:

$$O\left((\Delta x)^{\alpha} + (\Delta z)^{\beta}\right) \tag{53}$$

where Δx and Δz are equivalent cell sizes (for nonuniform grids) and α and β are the designed rates of the discretization schemes. When the discretization for one coordinate is fixed, for instance, if Δz and β are fixed, the observed rate for decreasing Δx would depend on the relative values of $(\Delta x)^{\alpha}$ and $(\Delta z)^{\beta}$. When $(\Delta x)^{\alpha}$ is decreased to an extent such that is becomes negligible compared to $(\Delta z)^{\beta}$, then the global error would only be proportional to $O((\Delta z)^{\beta})$. This explains the rate decrease observed when increasing N_x. The rate increase when increasing N_{col} can also be similarly explained: the global error was dominated by $(\Delta z)^{\beta}$. However, the low rate at the beginning was because the problem was still under-resolved as N_{col} was too small. A true rate was revealed when N_{col} was sufficiently large as it is an asymptotic property.

Projections of the Pareto fronts in Fig. 11(a) onto the N_x-N_{col} plane is shown in (b). From (b) a general trend could be revealed for all schemes: increasing N_x and N_{col} proportionally keeps the simulation to stay on the Pareto front. This was expected as both Δx and Δz in Eq. (53) needed to decrease at a similar rate ($\Delta x \sim \Delta z$, $\alpha = \beta$ in this case) to show convergence.

Regarding the runtime, increasing N_x or N_{col} led to an increased runtime overhead, however, this overhead increased at different rates. From the log–log–log plot of the runtime vs. N_x, N_{col} in Figure S2, we found that the runtime increased with an order of 1 when increasing N_{col} for all schemes. In contrast, the runtime was increasing faster at an order of 2 when increasing N_x for all schemes involved. This can be explained by the fact that CADET utilizes a highly optimized domain decomposition method in the z domain which has not yet been applied in the x domain.

Moments were used to calculate the volume-averaged mean size, total count and count of the fine particles which are defined as particles smaller than 10 μm in this test. Shown in Figure S9, the errors for these metrics decreased in a similar fashion to the normalized L1 norm when increasing N_x and N_{col}, which was not surprising as they were linear combinations of the moments calculated from the distribution itself and their global errors should converge in a similar way to the normalized L1 norm. As revealed in Fig. 12, the HR Koren scheme was found to be Pareto optimal for the mean size while all schemes including the upwind scheme showed similar performances for the total count and fine count. Another important observation here was that these Pareto fronts were different from those in Fig. 10(a) and a different optimal trajectory should be used if only these metrics were of interest.

The advantages of using analytical Jacobians compared to AD are briefly demonstrated in Table 1. Although the speed-up declined as N_x and N_{col} increased, simulations using analytical Jacobians were still generally one order faster than those using AD.

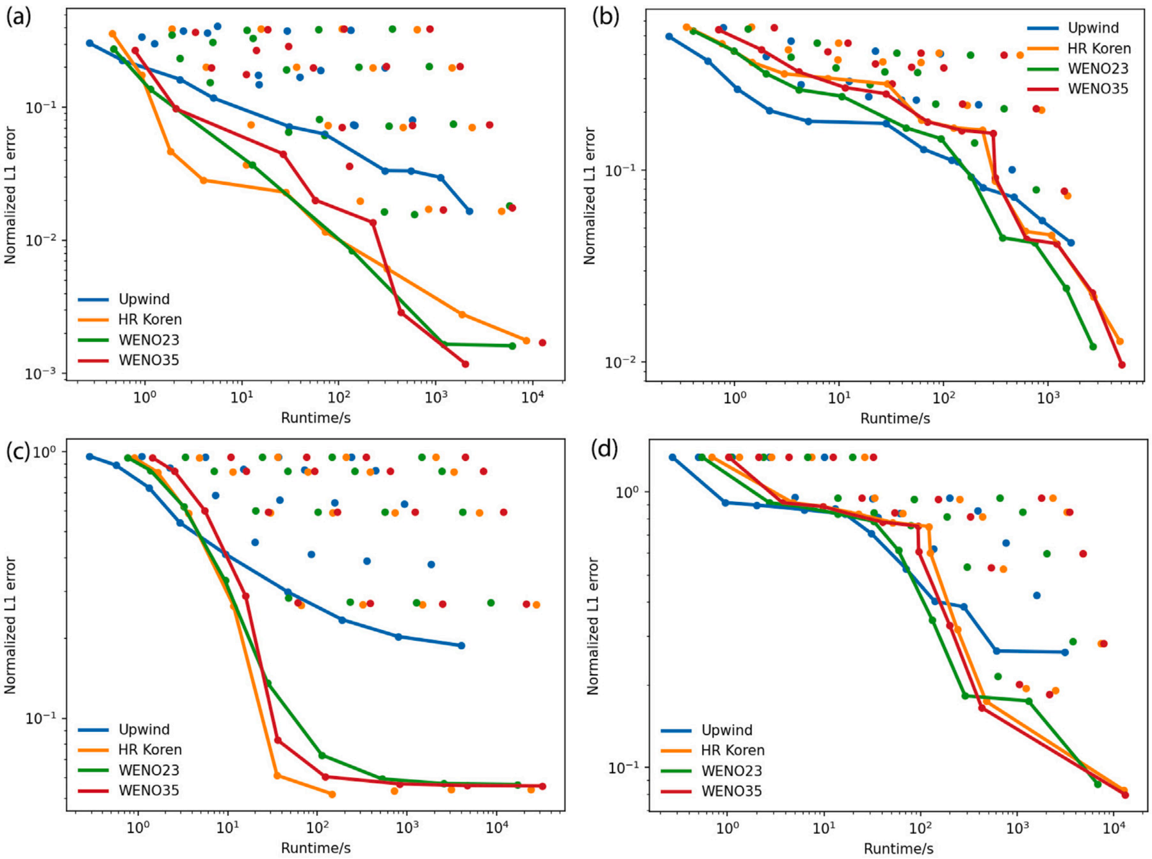

Fig. 10. Case 7: normalized L1 norm vs. runtime. A uniform grid is used for the external coordinate. Numerical schemes are indicated by color. Scatters are the results from the 5x5 grid. Solid lines are Pareto fronts of each scheme. Particles born (a) as critical nuclei on a logarithmic grid, (b) as critical nuclei on a uniform grid, (c) with an intrinsic log-normal distribution on a logarithmic grid, (d) with an intrinsic log-normal distribution on a uniform grid.

Table 1
Runtime using AD vs. analytical Jacobians for Case 7A. The same number of cells were used in both coordinates.

N_x, N_{col}	Upwind			HR Koren		
	AD	Analytical	Speed-up factor	AD	Analytical	Speed-up factor
10	1.22 s	0.06 s	20.33	2.68 s	0.07 s	38.29
20	6.63 s	0.20 s	33.15	17.49 s	0.40 s	43.73
40	39.46 s	1.97 s	20.03	119.86 s	5.63 s	21.29
80	243.70 s	19.56 s	12.46	859.43 s	59.37 s	14.48

N_x, N_{col}	WENO23			WENO35		
	AD	Analytical	Speed-up factor	AD	Analytical	Speed-up factor
10	2.88 s	0.07 s	41.14	5.43 s	0.06 s	49.36
20	20.89 s	0.40 s	52.23	41.26 s	0.31 s	61.58
40	119.37 s	4.21 s	28.35	304.97 s	3.32 s	41.27
80	918.65 s	48.18 s	19.07	2266.30 s	77.97 s	16.43

The impact of a uniform grid for the internal coordinate x was also tested, keeping everything else the same as in the above logarithmic grid case. The Pareto front for the uniform grid case is reported in Fig. 10(b) and the corresponding error and runtime plots can be found in Figure S6 and S3. In contrast to the logarithmic grid case where the upwind scheme showed the worst performance, it actually became the Pareto optimal for a higher error regime (about 0.1) while at a lower error regime it was superseded by high-order schemes which shared similar performances. Except for the upwind scheme whose error decreased slowly along the N_x and N_{col} coordinates at a rate of around 0.8, the errors for all high order schemes decreased at a faster rate with a maximum of 2 and 1 along N_x and N_{col} coordinates, respectively. The runtime for the high order schemes in the x coordinate increased at a rate of 2 while a rate of 1 was observed for the z coordinate.

For the scalar metric errors and Pareto front analysis in Figure S10 and S11: the mean size and total count errors had similar shapes to that of the normalized L1 norm. However, errors for the fines count did not strictly converge as we increased N_x or N_{col}. This might be explained by the inconsistency of the scheme that led to decreased or non-convergence of the local error combined with a forced cell search ($x_i < 10$ μm) that resulted in an irregular pattern for the number of cells considered for the calculation of the error. The Pareto front analysis showed that HR Koren and WENO23 were Pareto optimal for the mean size. Surprisingly, the upwind scheme dominated all other schemes for the total and fine particle counts. Similar to the logarithmic grid case, these Pareto fronts were different from those in Fig. 10(b), indicating that they had different optimal trajectories.

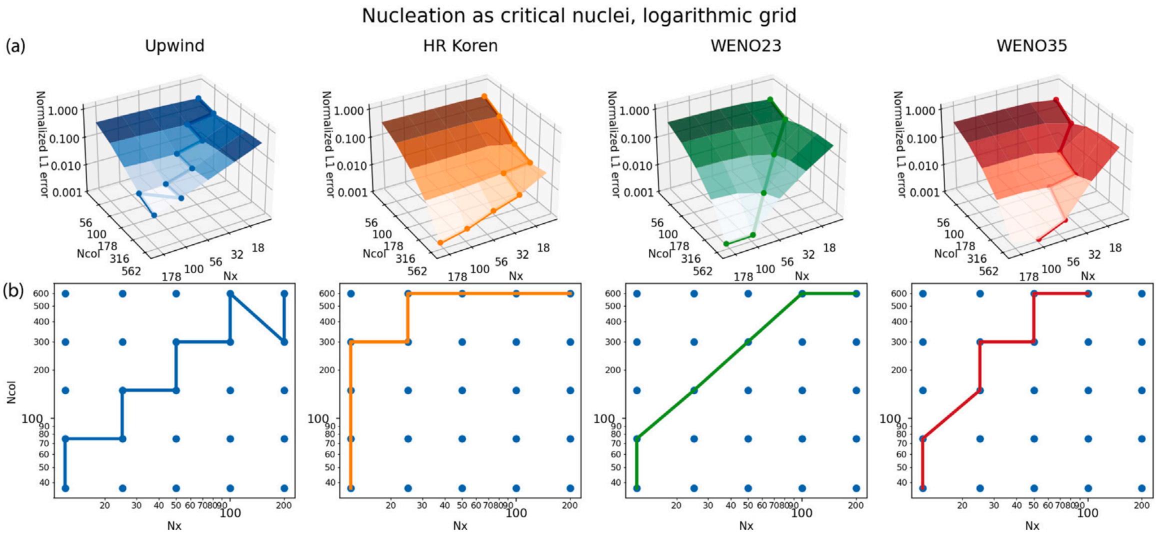

Fig. 11. (a): log–log–log surface plots of the normalized L1 norm vs. N_x and N_{col}. The Pareto optimal is highlighted; (b): projections of the Pareto optimal onto the N_x and N_{col} plane.

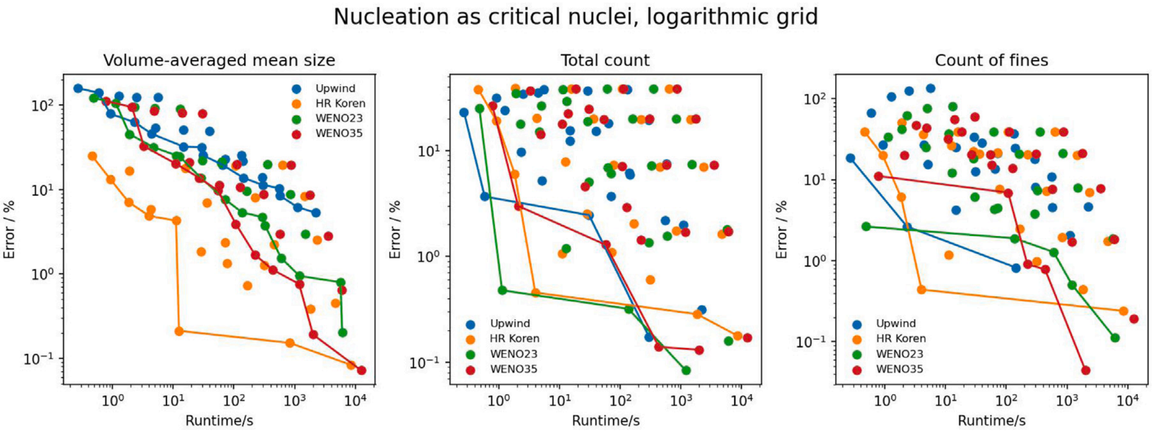

Fig. 12. Percent error vs. runtime for the evaluated metrics. Scatters are the evaluated points. Solid lines are the Pareto fronts.

6.7.2. *Case 7B: particles are born with an intrinsic log-normal distribution*

In case 7B, particles are born with an intrinsic log-normal distribution (52) ($y_0 = 0$, $A = 1$, $\omega = 0.3$, $x_{ct} = 4.$). Fig. 9(b) and (d) shows non-equilibrium solutions at $t = 80$ s and flow equilibrium solutions at the reactor outlet at $t = 200$ s. Similar to case 7 A, an insufficient N_{col} resulted in under-predictions of the number density distribution intensity and over-predictions of the amount of large particles, which was evident in the volume fraction distribution. Compared to case 7 A, an even more dramatic discrepancy in the volume fraction distribution was seen when N_{col} was insufficient, stressing its crucial role in reducing errors.

Error and runtime analyses were carried out for case 7B. Fig. 10(c) shows the HR Koren scheme was the Pareto front scheme for a normalized error smaller than ca. 0.5, but the upwind scheme was dominant for a larger error regime. Judging from Figure S7, the normalized L1 norm converged very slowly along the N_x coordinate. Similar to case 7 A, the slope along the N_x coordinate at $N_{col} = 400$ was gradually decreasing from (0.5, 0.2, 0.9, 0.5) to (0.1, 0.0, 0.0, 0.0) for the upwind, HR Koren, WENO23 and WENO35 schemes, respectively. In contrast, the error converged at a much faster rate along the N_{col} coordinate: the steepest slope at $N_x = 200$ was found to be (1.0, 2.3, 2.3, 2.3) for the upwind, HR Koren, WENO23 and WENO35 schemes, respectively. In terms of the runtime (Figure S4), increasing the number of cells in the internal coordinate x led to a bigger penalty than that in the external coordinate z with an order of around 2.2 for increasing N_x and an order of around 0.9 for increasing N_{col} for all schemes involved. Regarding the scalar metrics (Figure S12 and S13), the HR Koren scheme still resided on the Pareto front for the mean size. For the total particle count, similar to the normalized L1 norm, the upwind and HR Koren schemes were the Pareto optimal depending on the error regime. In contrast, the upwind scheme was dominant for the fine particle count errors.

When case 7B was tested on a uniform grid (Fig. 10(d)), similar performance was observed for all schemes. Similar to the observed performance for case 7 A, for a fixed N_{col}, the error converged slowly when increasing N_x, with a maximum order of 1.2 seen in WENO35. The error again converged faster for a fixed N_x when increasing N_{col} with a maximum of 1.8 seen in the WENO35. For all schemes involved, the runtime increased at an order of about 0.8 when increasing N_{col} and an order of about 2.0 when increasing N_x. Regarding the scalar metrics (Figure S14 and S15), all schemes performed equally well in reducing the errors for a given runtime.

7. Conclusions

In this article, we solved the population balance model coupled with a solute mass balance equation formulated for stirred tank and in a dispersive plug flow reactor formats in CADET. We implemented several widely-used expressions for the particle nucleation and growth constitutive equations. Due to the open source code of CADET, the mathematical expressions can be modified to accommodate different applications in different fields which apply population balances. A special population balance formulation that considers the case where the nuclei can be generated beyond the critical nuclei is also presented. A finite volume method with several flux reconstruction schemes including the upwind, HR Koren with the van Leer flux limiter, WENO23 and WENO35 schemes for arbitrary grids was implemented, and rigorously verified and numerically bench-marked. Analytical Jacobians associated with all flux reconstruction schemes were derived and implemented to reduce the runtime.

The fidelity of the numerical representation of each of the terms of the governing equations was carefully validated throughout seven test cases. We revisited and improved some of the existing test cases and generated several new test cases for the 1D and 2D PBM. Novel bench-marking methodologies were developed to test solver performances. These test cases shed light on appropriate flux reconstruction schemes and cell numbers to use depending on the chosen crystallization/precipitation mechanisms and initial conditions of the system.

For 1D cases, the WENO35 scheme was observed to be the optimal scheme to use when there is only growth of an initially smooth particle size distribution. If the initial distribution is sharp or the particles are born as critical nuclei, the WENO35 scheme was at best similar to and sometimes inferior to the HR Koren and WENO23 schemes due to either increased number of calculations involved or due to limitations of the boundary treatment. We further found that the use of logarithmic grids resulted in a higher computational burden and a slower convergence rate. The former was due to the grid refinement and extra computations for the scheme coefficients, while the latter might be attributed to the non-consistency of the finite volume scheme on nonuniform grids.

For 2D PBM cases, we found that an insufficient number of cells N_{col} in the external coordinate z led to under-predictions of the number density distribution intensity and over-predictions of the amount of large particles. By examining the normalized L1 norm under different cases, we found that it decreased quickly when increasing N_{col}, stressing its importance. Regarding the grid structure for x, the error decreased faster on a uniform grid than on a logarithmic grid for x. This is because the latter usually had smaller absolute values and errors in z were dominant, leading to apparent rate reductions for increasing N_x. We further found that on a logarithmic grid, increasing N_x and N_{col} proportionally helped the scheme to stay on the Pareto fronts. When increasing N_{col} and N_x, the runtime increased at a rate of two and one, respectively. Regarding the scalar metrics, their errors demonstrated different Pareto optimal behaviors. Sometimes the upwind scheme could also dominate the performance of high order schemes, but it would eventually give away if higher accuracy is desired. Errors for the fine particle count did not converge, possibly due to non-consistency of the finite volume scheme on nonuniform grids and(/or) a hard grid search. Overall, a logarithmic grid for x using the HR Koren scheme and increasing N_x and N_{col} proportionally should be the primary choice for 2D cases. However, caution must be taken if the scalar metrics are of special interest.

The second part of this work was devoted to incorporating the Smoluchowski equation to account for the aggregation and fragmentation processes in a stirred tank and dispersive plug flow reactor. We notice that solving the 2D PBM using the finite volume methods has led to a runtime increase of 1–2 orders of magnitude compared with 1D cases, which can be rather burdensome when solving complicated optimization problems.

In this work, the external and internal coordinates are discretized using the finite volume method. This can potentially be improved by applying high-order methods, such as a non-oscillatory discontinuous Galerkin method. Previous studies by Breuer et al. (2023) have shown up to two orders of magnitude of runtime speedup in the external coordinate. As both coordinates can be discretized separately, we expect even greater speedups in the 2D case. The method can potentially be further improved by concurrently discretizing both coordinates. This will require substantial changes to the core CADET code and will be the subject of future work.

CRediT authorship contribution statement

Wendi Zhang: Data curation, Formal analysis, Investigation, Methodology, Software, Validation, Visualization, Writing – original draft. **Todd Przybycien:** Conceptualization, Funding acquisition, Project administration, Resources, Supervision, Writing – review & editing. **Johannes Schmölder:** Data curation, Methodology, Software. **Samuel Leweke:** Methodology, Software. **Eric von Lieres:** Conceptualization, Methodology, Resources, Supervision, Writing – review & editing.

Declaration of competing interest

The authors declare that they have no known competing financial interests or personal relationships that could have appeared to influence the work reported in this paper.

Data availability

The code and data will be made available on GitHub.

Acknowledgments

Wendi Zhang was supported by the U.S. Food and Drug Administration, USA, Contract No. 75F40121C00111. Johannes Schmölder has received funding from the Innovative Medicines Initiative 2 Joint Undertaking, EU under grant agreement No 101007799 (Inno4Vac). Any opinions, findings, conclusions, or recommendations expressed in this material are those of the authors and do not necessarily reflect the views of the financial sponsors. We cordially thank Jan Michael Breuer for his valuable comments which improved the manuscript.

Appendix A. Supplementary data

Supplementary material related to this article can be found online at https://doi.org/10.1016/j.compchemeng.2024.108612.

References

Abegg, C.F., Stevens, J.D., Larson, M.A., 1968. Crystal size distributions in continuous crystallizers when growth rate is size dependent. AIChE J. 14 (1), 118–122. http://dx.doi.org/10.1002/aic.690140121.

Ahmed, N., Matthies, G., Tobiska, L., 2011. Finite element methods of an operator splitting applied to population balance equations. J. Comput. Appl. Math. 236 (6), 1604–1621. http://dx.doi.org/10.1016/j.cam.2011.09.025.

Alvarez, A.J., Myerson, A.S., 2010. Continuous plug flow crystallization of pharmaceutical compounds. Cryst. Growth Des. 10 (5), 2219–2228. http://dx.doi.org/10.1021/cg901496s.

Aràndiga, F., Baeza, A., Belda, A.M., Mulet, P., 2011. Analysis of WENO schemes for full and global accuracy. SIAM J. Numer. Anal. 49 (2), 893–915. http://dx.doi.org/10.1137/100791579, URL: http://epubs.siam.org/doi/10.1137/100791579.

Bansode, V., Gupta, P., Kateja, N., Rathore, A.S., 2022. Contribution of protein A step towards cost of goods for continuous production of monoclonal antibody therapeutics. J. Chem. Technol. Biotechnol. 97 (9), 2420–2433. http://dx.doi.org/10.1002/jctb.6686.

Barry, K., 1993. A robust upwind discretization method for advection, diffusion and source terms. Int. J. Numer. Methods Fluids 117–138, URL: https://onlinelibrary.wiley.com/doi/10.1002/fld.2700.

Benitez-Chapa, A.G., Nigam, K.D., Alvarez, A.J., 2020. Process intensification of continuous antisolvent crystallization using a coiled flow inverter. Ind. Eng. Chem. Res. 59 (9), 3934–3942. http://dx.doi.org/10.1021/acs.iecr.9b04160.

Bennett, M.K., Rohani, S., 2001. Solution of population balance equations with a new combined Lax- Wendroff/Crank-Nicholson method. Chem. Eng. Sci. 56 (23), 6623–6633. http://dx.doi.org/10.1016/S0009-2509(01)00314-1.

Breuer, J.M., Leweke, S., Schmölder, J., Gassner, G., von Lieres, E., 2023. Spatial discontinuous Galerkin spectral element method for a family of chromatography models in CADET. Comput. Chem. Eng. 177, 108340. http://dx.doi.org/10.1016/j.compchemeng.2023.108340, URL: https://www.sciencedirect.com/science/article/pii/S0098135423002107.

Burgstaller, D., Jungbauer, A., Satzer, P., 2019. Continuous integrated antibody precipitation with two-stage tangential flow microfiltration enables constant mass flow. Biotechnol. Bioeng. 116 (5), 1053–1065. http://dx.doi.org/10.1002/bit.26922.

Caillet, A., Sheibat-Othman, N., Fevotte, G., 2007. Crystallization of monohydrate citric acid. 2. Modeling through population balance equations. Cryst. Growth Des. 7 (10), 2088–2095. http://dx.doi.org/10.1021/cg0606343, URL: https://pubs.acs.org/doi/10.1021/cg0606343.

Calhoun, D., LeVeque, R.J., 2000. A cartesian grid finite-volume method for the advection-diffusion equation in irregular geometries. J. Comput. Phys. 157 (1), 143–180. http://dx.doi.org/10.1006/jcph.1999.6369.

Canning, T.F., Randolph, A.D., 1967. Some aspects of crystallization theory: Systems that violate McCabe's delta L law. AIChE J. 13 (1), 5–10. http://dx.doi.org/10.1002/aic.690130104.

Cravero, I., Semplice, M., 2016. On the accuracy of WENO and CWENO reconstructions of third order on nonuniform meshes. J. Sci. Comput. 67 (3), 1219–1246. http://dx.doi.org/10.1007/s10915-015-0123-3, arXiv:1503.00736.

Diskin, B., Thomas, J.L., 2010. Notes on accuracy of finite-volume discretization schemes on irregular grids. Appl. Numer. Math. 60 (3), 224–226. http://dx.doi.org/10.1016/j.apnum.2009.12.001.

Frawley, P.J., Mitchell, N.A., Ó'Ciardhá, C.T., Hutton, K.W., 2012. The effects of supersaturation, temperature, agitation and seed surface area on the secondary nucleation of paracetamol in ethanol solutions. Chem. Eng. Sci. 75, 183–197. http://dx.doi.org/10.1016/j.ces.2012.03.041.

Garside, J., Jančić, S.J., 1976. Growth and dissolution of potash alum crystals in the subsieve size range. AIChE J. 22 (5), 887–894. http://dx.doi.org/10.1002/aic.690220512.

Gershon, N.D., Nir, A., 1969. Effects of boundary conditions of models on tracer distribution in flow through porous mediums. Water Resour. Res. 5 (4), 830–839. http://dx.doi.org/10.1029/WR005i004p00830, URL: http://doi.wiley.com/10.1029/WR005i004p00830.

Gu, Q., Li, Z., Coffman, J.L., Przybycien, T.M., Zydney, A.L., 2020. High throughput solubility and redissolution screening for antibody purification via combined PEG and zinc chloride precipitation. Biotechnol. Prog. 36 (6), http://dx.doi.org/10.1002/btpr.3041.

Gunawan, R., Fusman, I., Braatz, R.D., 2004. High resolution algorithms for multidimensional population balance equations. AIChE J. 50 (11), 2738–2749. http://dx.doi.org/10.1002/aic.10228.

Harten, A., Engquist, B., Osher, S., Chakravarthy, S.R., 1987. Uniformly High Order Accurate Essentially Non-Oscillatory Schemes, III. Springer.

Hermanto, M.W., Braatz, R.D., Chiu, M.-S., 2009. High-order simulation of polymorphic crystallization using weighted essentially nonoscillatory methods. AIChE J. 55 (1), 122–131. http://dx.doi.org/10.1002/aic.11644, URL: https://onlinelibrary.wiley.com/doi/10.1002/aic.11644.

Hou, J., Simons, F., Hinkelmann, R., 2012. Improved total variation diminishing schemes for advection simulation on arbitrary grids. Internat. J. Numer. Methods Fluids 70 (3), 359–382. http://dx.doi.org/10.1002/fld.2700, URL: https://onlinelibrary.wiley.com/doi/10.1002/fld.2700.

Hounslow, M.J., 1990. A Discretized Population Balance for Simultaneous Nucleation, Growth and Aggregation (Ph.D. thesis). University of Adelaide, URL: https://hdl.handle.net/2440/19087.

Hulburt, H., Katz, S., 1964. Some problems in particle technology. Chem. Eng. Sci. 19 (8), 555–574. http://dx.doi.org/10.1016/0009-2509(64)85047-8.

Jiang, M., Braatz, R.D., 2019. Designs of continuous-flow pharmaceutical crystallizers: Developments and practice. CrystEngComm 21 (23), 3534–3551. http://dx.doi.org/10.1039/c8ce00042e.

Jiang, G.-S., Shu, C.-W., 1996. Efficient implementation of weighted ENO schemes. J. Comput. Phys. 126 (1), 202–228. http://dx.doi.org/10.1006/jcph.1996.0130.

Kumar, J., Peglow, M., Warnecke, G., Heinrich, S., 2008. An efficient numerical technique for solving population balance equation involving aggregation, breakage, growth and nucleation. Powder Technol. 182 (1), 81–104. http://dx.doi.org/10.1016/j.powtec.2007.05.028.

Kumar, S., Ramkrishna, D., 1997. On the solution of population balance equations by discretization—III. Nucleation, growth and aggregation of particles. Chem. Eng. Sci. 52 (24), 4659–4679. http://dx.doi.org/10.1016/S0009-2509(97)00307-2.

Larson, M.A., White, E.T., Ramanarayanan, K.A., Berglund, K.A., 1985. Growth rate dispersion in MSMPR crystallizers. AIChE J. 31 (1), 90–94. http://dx.doi.org/10.1002/aic.690310110.

van Leer, B., 1985. Upwind-difference methods for aerodynamic problems governed by the Euler equations. In: Large-Scale Comput. Fluid Mech.. pp. 327–336.

LeVeque, R.J., 2002. Finite Volume Methods for Hyperbolic Problems. Cambridge University Press, http://dx.doi.org/10.1017/CBO9780511791253.

Leweke, S., von Lieres, E., 2018. Chromatography Analysis and Design Toolkit (CADET). Comput. Chem. Eng. 113, 274–294. http://dx.doi.org/10.1016/j.compchemeng.2018.02.025.

Li, Z., Gu, Q., Coffman, J.L., Przybycien, T., Zydney, A.L., 2019. Continuous precipitation for monoclonal antibody capture using countercurrent washing by microfiltration. Biotechnol. Prog. 35 (6), 1–8. http://dx.doi.org/10.1002/btpr.2886.

Lim, Y.I., Le Lann, J.M., Meyer, X.M., Joulia, X., Lee, G., Yoon, E.S., 2002. On the solution of Population Balance Equations (PBE) with accurate front tracking methods in practical crystallization processes. Chem. Eng. Sci. 57 (17), 3715–3732. http://dx.doi.org/10.1016/S0009-2509(02)00236-1.

Lin, Y., Lee, K., Matsoukas, T., 2002. Solution of the population balance equation using constant-number Monte Carlo. Chem. Eng. Sci. 57 (12), 2241–2252. http://dx.doi.org/10.1016/S0009-2509(02)00114-8.

Liu, X.-D., Osher, S., Chan, T., 1994. Weighted essentially non-oscillatory schemes. J. Comput. Phys. 115 (1), 200–212. http://dx.doi.org/10.1006/jcph.1994.1187, URL: http://link.springer.com/10.1007/978-3-642-60543-7_12.

Mahoney, A.W., Ramkrishna, D., 2002. Efficient solution of population balance equations with discontinuities by finite elements. Chem. Eng. Sci. 57 (7), 1107–1119. http://dx.doi.org/10.1016/S0009-2509(01)00427-4.

Majumder, A., Kariwala, V., Ansumali, S., Rajendran, A., 2012. Lattice Boltzmann method for multi-dimensional population balance models in crystallization. Chem. Eng. Sci. 70, 121–134. http://dx.doi.org/10.1016/j.ces.2011.04.041.

Mantzaris, N.V., Daoutidis, P., Srienc, F., 2001. Numerical solution of multi-variable cell population balance models. II. Spectral methods. Comput. Chem. Eng. 25 (11–12), 1441–1462. http://dx.doi.org/10.1016/S0098-1354(01)00710-4.

Marchal, P., David, R., Klein, J.P., Villermaux, J., 1988. Crystallization and precipitation engineering-I. An efficient method for solving population balance in crystallization with agglomeration. Chem. Eng. Sci. 43 (1), 59–67. http://dx.doi.org/10.1016/0009-2509(88)87126-4.

Marchisio, D.L., Pikturna, J.T., Fox, R.O., Vigil, R.D., Barresi, A.A., 2003. Quadrature method of moments for population-balance equations. AIChE J. 49 (5), 1266–1276. http://dx.doi.org/10.1002/aic.690490517.

Mason, M., Weaver, W., 1924. The settling of small particles in a fluid. Phys. Rev. 23 (3), 412–426. http://dx.doi.org/10.1103/PhysRev.23.412, URL: https://link.aps.org/doi/10.1103/PhysRev.23.412.

McCabe, W.L., 1929. Crystal growth in aqueous solutions: I—Theory. Ind. Eng. Chem. 21 (1), 30–33. http://dx.doi.org/10.1021/ie50229a008.

Mesbah, A., Kramer, H.J., Huesman, A.E., Van den Hof, P.M., 2009. A control oriented study on the numerical solution of the population balance equation for crystallization processes. Chem. Eng. Sci. 64 (20), 4262–4277. http://dx.doi.org/10.1016/j.ces.2009.06.060.

Motz, S., Mitrović, A., Gilles, E.D., 2002. Comparison of numerical methods for the simulation of dispersed phase systems. Chem. Eng. Sci. 57 (20), 4329–4344. http://dx.doi.org/10.1016/S0009-2509(02)00349-4.

Myerson, A.S., Erdemir, D., Lee, A.Y. (Eds.), 2002. Handbook of Industrial Crystallization, third ed. Elsevier, http://dx.doi.org/10.1016/B978-0-7506-7012-8.X5000-9.

Nagy, Z.K., Fujiwara, M., Braatz, R.D., 2008. Modelling and control of combined cooling and antisolvent crystallization processes. J. Process Control 18 (9), 856–864. http://dx.doi.org/10.1016/j.jprocont.2008.06.002.

Nishikawa, H., 2014. First-, second-, and third-order finite-volume schemes for diffusion. J. Comput. Phys. 256, 791–805. http://dx.doi.org/10.1016/j.jcp.2013.09.024.

Pilon, L., Viskanta, R., 2003. Modified method of characteristics for solving population balance equations. Internat. J. Numer. Methods Fluids 42 (11), 1211–1236. http://dx.doi.org/10.1002/fld.586.

Püttmann, A., Schnittert, S., Leweke, S., von Lieres, E., 2016. Utilizing algorithmic differentiation to efficiently compute chromatograms and parameter sensitivities. Chem. Eng. Sci. 139, 152–162. http://dx.doi.org/10.1016/j.ces.2015.08.050.

Püttmann, A., Schnittert, S., Naumann, U., von Lieres, E., 2013. Fast and accurate parameter sensitivities for the general rate model of column liquid chromatography. Comput. Chem. Eng. 56, 46–57. http://dx.doi.org/10.1016/j.compchemeng.2013.04.021.

Qamar, S., Elsner, M.P., Angelov, I.A., Warnecke, G., Seidel-Morgenstern, A., 2006. A comparative study of high resolution schemes for solving population balances in crystallization. Comput. Chem. Eng. 30 (6–7), 1119–1131. http://dx.doi.org/10.1016/j.compchemeng.2006.02.012.

Qamar, S., Warnecke, G., Elsner, M.P., 2009. On the solution of population balances for nucleation, growth, aggregation and breakage processes. Chem. Eng. Sci. 64 (9), 2088–2095. http://dx.doi.org/10.1016/j.ces.2009.01.040.

Ramkrishna, D., 2000. Population Balances: Theory and Applications to Particulate Systems in Engineering. Academic Press, p. 355. http://dx.doi.org/10.1016/B978-0-12-576970-9.X5000-0.

Randolph, A., Larson, M., 1988. Theory of Particulate Processes, second ed. Elsevier, p. 369. http://dx.doi.org/10.1016/B978-0-12-579652-1.X5001-7.

Randolph, A.D., White, E.T., 1977. Modeling size dispersion in the prediction of crystal-size distribution. Chem. Eng. Sci. 32 (9), 1067–1076. http://dx.doi.org/10.1016/0009-2509(77)80144-9.

Raphael, M., Rohani, S., 1999. Sunflower protein precipitation in a tubular precipitator. Can. J. Chem. Eng. 77 (3), 540–554. http://dx.doi.org/10.1002/cjce.5450770315.

Rothstein, F., 1993. Differential precipitation of proteins. In: Harrison, R.G. (Ed.), Protein Purif. Process Eng., first ed. Routledge, p. 94. http://dx.doi.org/10.1201/9780203741733, URL: https://www.taylorfrancis.com/books/9781351421010.

Saleemi, A.N., Rielly, C.D., Nagy, Z.K., 2012. Comparative investigation of supersaturation and automated direct nucleation control of crystal size distributions using ATR-UV/vis spectroscopy and FBRM. Cryst. Growth Des. 12 (4), 1792–1807. http://dx.doi.org/10.1021/cg201269c.

Shu, C.-W., 1998. Essentially Non-Oscillatory and Weighted Essentially Non-Oscillatory Schemes for Hyperbolic Conservation Laws, (no. 97), pp. 325–432. http://dx.doi.org/10.1007/BFb0096355, URL: http://link.springer.com/10.1007/BFb0096355.

Smit, J., Van Sint Annaland, M., Kuipers, J.A., 2005. Grid adaptation with WENO schemes for non-uniform grids to solve convection-dominated partial differential equations. Chem. Eng. Sci. 60 (10), 2609–2619. http://dx.doi.org/10.1016/j.ces.2004.12.017.

Smith, M., Matsoukas, T., 1998. Constant-number Monte Carlo simulation of population balances. Chem. Eng. Sci. 53 (9), 1777–1786. http://dx.doi.org/10.1016/S0009-2509(98)00045-1.

Srisanga, S., Flood, A.E., Galbraith, S.C., Rugmai, S., Soontaranon, S., Ulrich, J., 2015. Crystal growth rate dispersion versus size-dependent crystal growth: Appropriate modeling for crystallization processes. Cryst. Growth Des. 15 (5), 2330–2336. http://dx.doi.org/10.1021/acs.cgd.5b00126.

Svärd, M., Gong, J., Nordström, J., 2008. An accuracy evaluation of unstructured node-centred finite volume methods. Appl. Numer. Math. 58 (8), 1142–1158. http://dx.doi.org/10.1016/j.apnum.2007.05.002.

Turkel, E., 1986. Accuracy of schemes with nonuniform meshes for compressible fluid flows. Appl. Numer. Math. 2 (6), 529–550.

van Genuchten, M., Alves, W., 1984. Analytical Solutions of the One-Dimensional Convective-Dispersive Solute Transport Equation. In: Agric. Water Manag., vol. 9, (no. 1), pp. 79–80. http://dx.doi.org/10.1016/0378-3774(84)90020-9.

von Lieres, E., Andersson, J., 2010. A fast and accurate solver for the general rate model of column liquid chromatography. Comput. Chem. Eng. 34 (8), 1180–1191. http://dx.doi.org/10.1016/j.compchemeng.2010.03.008.

Wellner, J., 2016. Comparison of finite volume high-order schemes for the two-dimensional Euler equations. In: Proceedings of the 7th European Congress on Computational Methods in Applied Sciences and Engineering.

Wood, B., Girard, K.P., Polster, C.S., Croker, D.M., 2019. Progress to date in the design and operation of continuous crystallization processes for pharmaceutical applications. Org. Process Res. Dev. 23 (2), 122–144. http://dx.doi.org/10.1021/acs.oprd.8b00319.

Woodward, C.S., Balos, C.J., 2021. User Documentation for Idas V4.7.0. Technical Report, Center for Applied Scientific Computing, Lawrence Livermore National Laboratory, p. 465.

Xing, Y., Shu, C.W., 2006. High order well-balanced finite volume WENO schemes and discontinuous Galerkin methods for a class of hyperbolic systems with source terms. J. Comput. Phys. 214 (2), 567–598. http://dx.doi.org/10.1016/j.jcp.2005.10.005.

Yuan, C., Laurent, F., Fox, R.O., 2012. An extended quadrature method of moments for population balance equations. J. Aerosol Sci. 51, 1–23. http://dx.doi.org/10.1016/j.jaerosci.2012.04.003.